Chapter-5

5 Deciphering Interaction between Chlorophyll functionalized Carbon Quantum Dots with Arsenic and Mercury Toxic Metals in Water as Highly Sensitive Dual-probe Sensor

5.1 Introduction

5.1.1 Source of Water Pollution

Water pollution is one of the major man-made crises that is now threatening the earth's ecosystem. Every day approximately 2 million tons of industrial and agricultural sewage waste are discharged into water bodies worldwide, posing a serious risk to humans, plants, and wildlife [182]. There are different types of water pollutants like domestic wastes, chemical waste, insecticides and herbicides, food processing waste, volatile organic compounds (VOCs), heavy metals (lead, arsenic, mercury, cadmium, chromium, etc.). Out of these, heavy metal pollution is the most widespread and harmful. Heavy metal pollutants are commonly produced by geogenic, industrial, pharmaceutical, and agricultural (insecticides and herbicides) processes. Industrial waste from mining and extraction, smelting, foundries, batteries, metal plating, and other metal-based processes is the biggest source of heavy metal contamination of our waterways. In recent years, improper recycling of electronic waste is also causing heavy metal contamination of groundwater. Heavy metals present in the earth's crust can enter water resources through natural processes. Arsenic is widely present in over 200 minerals, out of which some of them are volatile and readily soluble in water, leading to the steady leaching of arsenic into groundwater. Similarly, Mercury, also present in rocks, is released during mining activities. Due to their non-biodegradable nature, trace amounts of heavy metals can readily accumulate in the food chain posing a severe health risk for humans. Methylmercury, a highly toxic form of mercury, produced by bacteria in the water is absorbed by plankton which then builds up in fish, shellfish, and humans consuming these contaminated fish and shellfish. Prolonged exposure to contaminated food/water can cause skin, nervous, respiratory, endocrinological, and immune disorders including cancer. Their toxicity depends on many factors like the dose of exposure, and chemical species, as well as the age, gender, genetics, and nutritional status of exposed individuals [183]. Unsafe drinking water still is the leading cause of death each year, hence it is of paramount importance to detect these toxic metals and remove them from water meant for human consumption.

5.1.2 Techniques for detection of heavy metals in water

The first step toward addressing this issue is the detection of trace amounts of toxic metals in water. The most common method of detecting the heavy metal contaminants in the water is by spectroscopic techniques like atomic absorption spectroscopy, atomic emission spectroscopy, and mass spectroscopy [184]. These techniques provide a limit of detection well below the WHO/EPA regulations but these laboratory-based techniques are slow and expensive, require bulky instrumentation, extensive sample preparation, and so are not suitable for onsite diagnostics [185]. Alternative low-cost methods like surface-enhanced Raman spectroscopy, electrochemical methods, chemiluminescence, and fluorescence spectroscopy are also being used. Compared to other methods fluorescence methods have a fast response, high sensitivity, specificity, and accuracy [186]. It is also relatively simple and does not require sophisticated systems for operation. Proof of concept fluorescence-based portable sensors has also been developed [185]. To detect non-fluorescent analytes, fluorescent probes are used that change their emission in response to binding with the analyte. Many fluorescent probes have been designed and developed including organic dyes, metal-organic hybrid material, organic polymer, and fluorescent proteins [187][188]. Recently nanomaterials such as carbon quantum dots (CQD), semiconductor quantum dots (QD), metal nanoparticles, graphene (G), graphene oxide (GO), transition metal dichalcogenides (TMDC), and more, have been used as fluoroprobes for detection systems [189][190].

5.1.3 Properties of CQDs

Carbon Quantum dots (CQD) is preferred over other nanomaterials due to their unique optoelectronic properties, high quantum yields, good biocompatibility, low toxicity, high photostability, aqueous phase stability, and facile synthesis [191]. CQDs can be synthesized using the top-down or bottom-up method. In bottom-up methods, like hydrolysis, hydrothermal, solvothermal, and microwave-assisted pyrolysis, different precursors like small organic molecules, polymers, and natural biomaterials are used [192]. Plant extracts from neem, basil and other medicinal plants, containing various bioactive compounds have been used to synthesize CQDs [193] . It has been shown that the neem leaf (*Azadirachta Indica*) have better supercapacitor properties than Ashoka (*Saraca Asoca*) due to the presence of the bioactive components present in *Azadirachta Indica* [194]. Solid biowastes are also used to synthesize CQDs. Fluorescent CQDs were also synthesized from banana peel which was used for in vivo imaging [30]. The use of various natural organic precursors endows the CQDs with diverse surface functional groups, resulting in unique optoelectronic properties [195][196][197][198]. This rich surface chemistry of CQDs can thus be utilized for the detection of analytes with high sensitivity and selectivity.

In this Chapter, we report the use of functionalized CQDs for selective detection of Hg^+ and As^{3+} ions. The CQDs have been synthesized from banana leaves (widely available in our area) using the hydrothermal growth method. The synthesis temperature was varied to tune the surface functionalization of CQDs. The CQDs synthesized at higher temperatures (beyond 200°C), exhibit broad emission peaks at 480 nm characteristic of CQDs. The CQDs synthesized at low temperatures (120°C and 160°C), exhibit new emission peaks at 677 nm and 725 nm. We hypothesize that at low temperatures due to the incomplete decomposition of organic precursors we get chlorophyll functionalized CQDs, while at high temperatures (beyond 200°C) the precursor molecules are completely decomposed to form only CQDs. To prove our hypothesis, we conducted systematic X-ray photoelectron spectroscopy (XPS) measurements to decipher the evolution of the chemical composition of the CQDs as a function of synthesis temperature. The CQDs synthesized at 160°C have been used to fabricate ON/OFF type of optical sensors for detecting toxic heavy metals. In the presence of Hg^+ ions, the fluorescence bands at 677 nm get quenched while in the case of As^{3+} ions the band at 677 nm is enhanced. This enhancement or quenching is only observed for chlorophyll functionalized CQDs synthesized at 160°C and not for CQDs synthesized at 200°C or 230°C. There is a synergistic effect between CQDs and the chlorophyll functional group which is improving the interaction of As^{3+} and Hg^+ with ChlCQDs leading to strong enhancement or quenching of fluorescence. To understand the interaction between the CQDs and metal ions, UV-vis and XPS measurements were conducted after the addition of metal ions. DFT calculations were also conducted to gain atomic-level insight into the interactions of As^{3+} and Hg^+ with the different functional groups present on the ChlCQD surface.

5.2 Results and Discussion

The CQDs were characterized by a suite of analytical techniques to get information about their structural, optical, and chemical properties. Then they were utilized for the detection of Hg^+ and As^{3+} ions.

5.2.1 Optical characterization of CQDs

Figure *5.1* (a) shows the UV Vis absorption spectra of the banana leaf extract solution and the CQDs synthesized at temperatures 120°C, 160°C, 200°C, and 230°C. The absorbance spectra have been staggered for better visualization. For the extract, we observe a peak at 417 nm and 677 nm. For CQDs synthesized at 120°C, we observe sharp peaks at 225 nm, broad peaks at 275 nm, and weak peaks at 417 nm and 677 nm. As the synthesis temperature is increased to 160°C, there seems to be a convolution of peaks between 275 nm and 417 nm, while the peak at 225 nm vanishes. The absorbance spectra at 160°C show that a new complex structure forming which has distinct absorbance spectra quite different from CQDs. When the synthesis temperature is increased further to 200°C and 230°C, the peak at 225 nm reappears while 275 nm remains unchanged but the intensity of the peaks at 417 nm and 677 nm completely vanishes. The absorbance peak at 225 nm and 275 nm is a common feature of the CQDs synthesized at all temperatures, while the absorbance peak at 417 nm and 677 nm is only present for the CQDs synthesized at 120°C and 160°C. Absorption peaks due to π- π^* transitions of C=C bond in graphene and graphene oxide are observed around 250-270 nm and 230 nm, respectively [199]. There is also a peak at 280 nm due to absorption for to n-π^* transition of C-O bonds. So in our case the absorbance peak at 225 nm and 275 nm can be attributed to the π–π^* transition of the C═C bond and the convolution of absorption peaks from π- π^* and n- π^* transitions of C═C bond and C=O bond respectively [200]. Observation of these absorption bands due to the π-plasmon indicates the onset of carbonization of the precursor into graphitic-like nanostructures. The absorption peak in the red region around 417 nm and 677 nm, is similar to that of banana leaf extract solution. Chlorophyll, a magnesium porphyrin derivative, has an extensive π-electron system, and the electronic transitions between π and π* orbitals of the chlorophyll macrocycle give rise to large absorption bands around 600-800 nm (Q band), and 380-430 nm (Soret or B band) [201] [202][203]. Therefore, we have also assigned the peaks at 417 nm and 677 nm to the B and Q band of chlorophyll respectively.

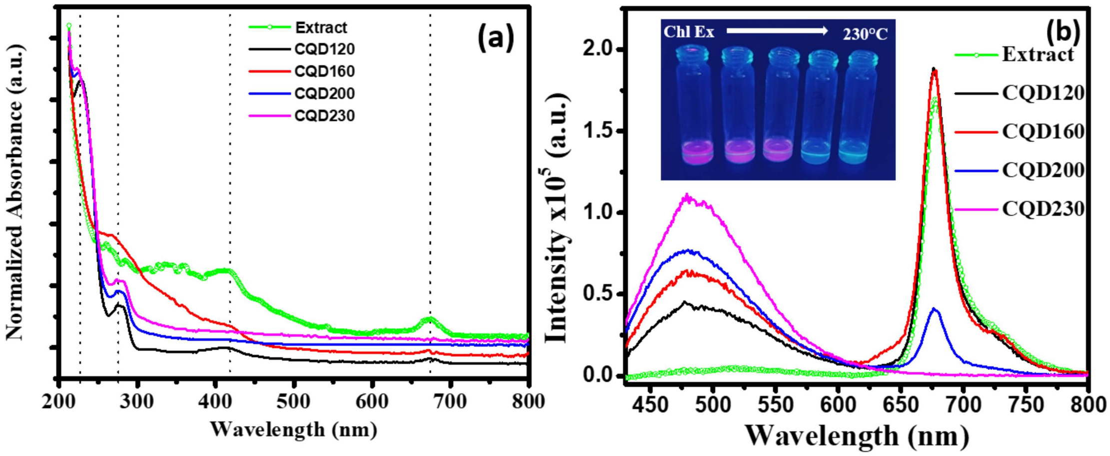

Figure 5.1 Optical Characterization of CQDs synthesized at different temperatures (a) UV-Vis absorbance spectra of CQDs at concentration 0.2 μg/ml. For comparison, the absorbance spectra of chlorophyll extract is also shown. (b) Emission spectra of the CQDs (concentration 0.02 μg/ml) were recorded using 410 nm excitation. Inset: The evolution of the emission color for 200 μg/ml CQDs

The band gaps of these CQDs were calculated using the Tauc plot (Figure *5.2* (a)). The band gaps for CQDs synthesized at 120°C, 160°C, 200°C, and 230°C are 4.93 eV, 5.05 eV, 4.93 eV, and 4.92 eV respectively. Figure *5.1* (b) shows the fluorescence spectra of the banana leaf extract and CQDs (1 μg/ml) acquired with excitation of 410 nm. For the banana leaf extract solution, we observe a weak peak at 520 nm and a large peak at 677 nm. The emission spectra for CQDs at 120°C, 160°C, and 200°C exhibited a broad emission peak at 480 nm and a sharp emission peak at 677 nm with a weak shoulder at 725 nm. Typically, CQDs have been reported to have single broad emission peaks around ~ 450 nm [204]. The peaks at 677 nm and 725 nm correspond to emissions from chlorophyll [205]. Similar dual emissions with peaks at the blue/green region and red region have previously been reported for CQDs synthesized using biomass [206][207]. As the synthesis temperature is increased from 120°C to 230°C, the intensity of the emission peak at 480 nm peak increases while the intensity at 677 nm decreases. At 230°C the intensity of the 677 nm peak completely vanishes. The ratio of intensities $I_{480\ nm}/I_{677\ nm}$ at 120°C, 160°C, 200°C is 0.23, 0.34, 1.89 respectively. All the above absorption and emission spectra were recorded for a CQD concentration of 0.2 µg/ml. At this low concentration, the change in emission color under UV light illumination can hardly be registered with the naked eye. However, when the concentration of CQDs is increased to 200 µg/ml, the changes in the emission color of CQDs synthesized at 120°C, 160°C, 180°C, and 230°C can be detected with the naked eye. The inset of Figure *5.1* (b) shows the change in emission color of the solution CQD solution from pink to blue under UV light illumination. The starting precursor solution also exhibits similar pink color as the CQDs prepared at 120°C and 160°C. The color of the CQD solution changes blue when the synthesis temperature is increased to 200°C and above. It is apparent that the chlorophyll moiety which is giving rise to the pink color is getting decomposed at a higher temperature. In any hydrothermal process, the precursors usually undergo a series of reaction steps (dehydration, condensation, polymerization, carbonization, and finally graphitization) to produce CQDs. In this method, the synthesis temperature determines the degree of carbonization and graphitization of the

CQDs [208]. Our result thus suggests that at low temperatures (120°C and 160°C) there is incomplete carbonization of chlorophyll which leads to chlorophyll functionalized CQDs (ChlCQD). These chlorophyll functionalized CQDs have two fluorescent centers one is the carbon core and the second is the chlorophyll moiety on the surface which gives rise to fluorescence in the near blue and red region respectively. The carbonization is complete at 230°C where we get an optical signature of CQDs only. These CQDs at 200°C and 230°C are more like graphene oxide quantum dots (GOQD) since they still have many oxygen-containing surface functional groups [209]. However, for our discussion purposes, we will continue to label them as CQDs.

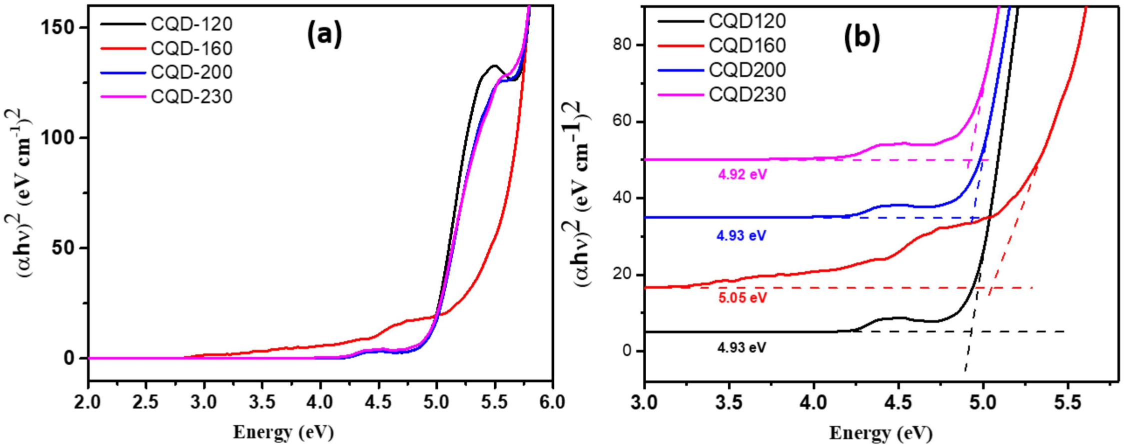

Figure 5.2 (a) Tauc Plot of the CQDs synthesized at 120°C, 160°C, 200°C and 230°C. In panel (b) the spectra have been staggered for better visualization

5.2.2 Chemical composition of CQDs

To get a better understanding of the evolution of the chemical composition of CQDs as a function of synthesis temperature Fourier Transform Infra-Red Spectroscopy (FTIR) and X-ray Photoelectron spectroscopic measurements were conducted. Figure *5.3* (a) shows the evolution of the FTIR spectra as a function of synthesis temperature. From the FTIR spectra, we observe broad absorption bands between 3200 - 3800 cm^{-1} characteristic of overlapping O-H and N-H stretching vibrations [210]. The sharp absorption bands observed at 2926 cm^{-1} and 2854 cm^{-1} are assigned to CH_2 groups. The broad but weak bands from 1496 cm^{-1} to 1340 cm^{-1} may be due to overlapping absorption peaks from C=O, C=C, and N-O groups. Carbonyl groups C=O have stretching modes at 1727 cm^{-1} and 1636 cm^{-1} while there is a C=C or aromatic ring stretch mode at 1636 cm^{-1} [211]. The peak at 1285 cm^{-1} can be assigned to C-N stretching. There are also multiple bands in the range 1120 cm^{-1} to 1020 cm^{-1} corresponding to C-H in-plane bending vibrations of aromatic compounds. The peak at 1035 cm^{-1} can also be due to C-O vibrations. From the FTIR spectra, it is evident that the CQDs are decorated with many oxygen-containing and some nitrogen containing functional groups. The presence of a large number of oxygen-containing functional groups endowed CQDs with excellent water solubility.

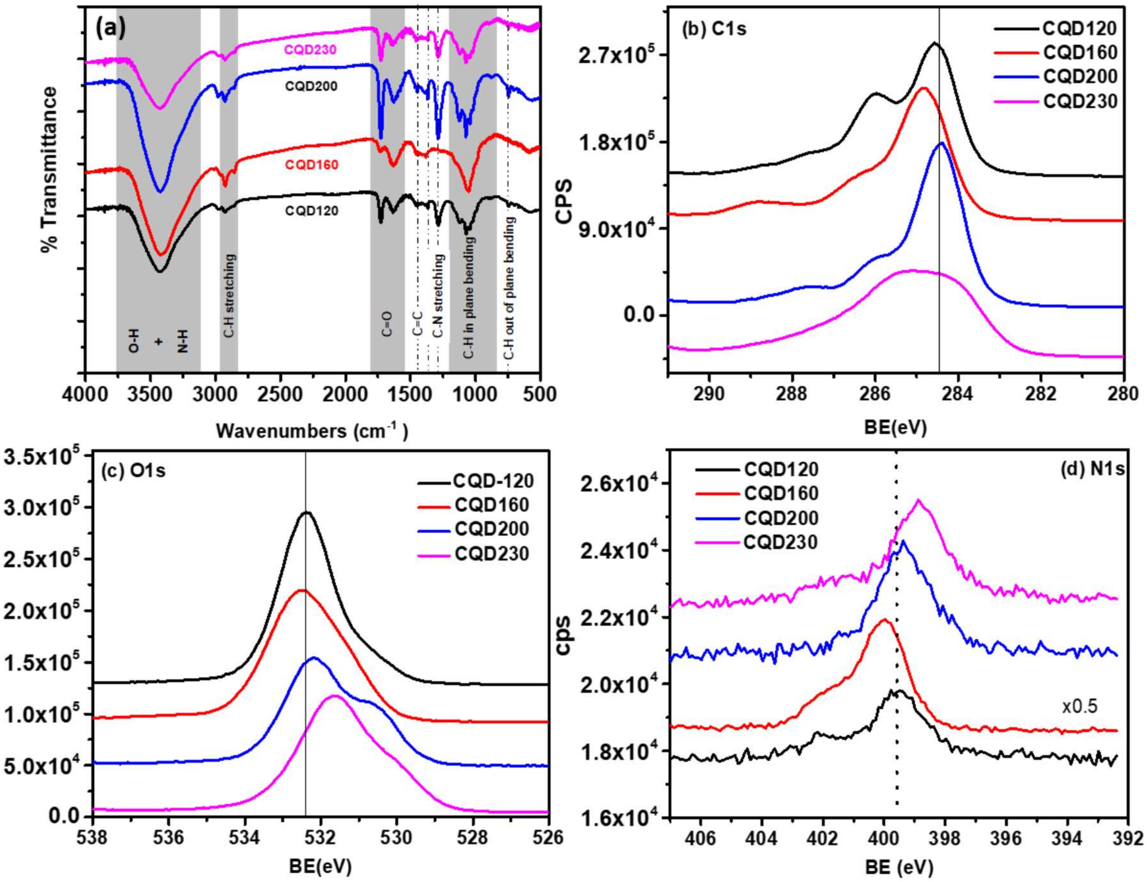

Figure 5.3 Spectroscopic characterization of CQDs synthesized at different temperatures- (a) FTIR spectra of the CQDs. High-resolution XPS spectra of (b) C1s (c) O1s (d) N1s photoelectron peaks (120°C, 160°C, 200°C, 230°C)

The XPS survey spectrum of these CQDs is shown in Figure *5.4*. From the survey spectrum, we see that the CQDs are mainly composed of C, N, and O species with the percentage of N being the smallest. We did not detect any signature of Mg^{2+} ion in the XPS scans. It could mean that either there are not enough Mg^{2+} ions in the probed samples or the Mg^{2+} is lost during hydrothermal processing.

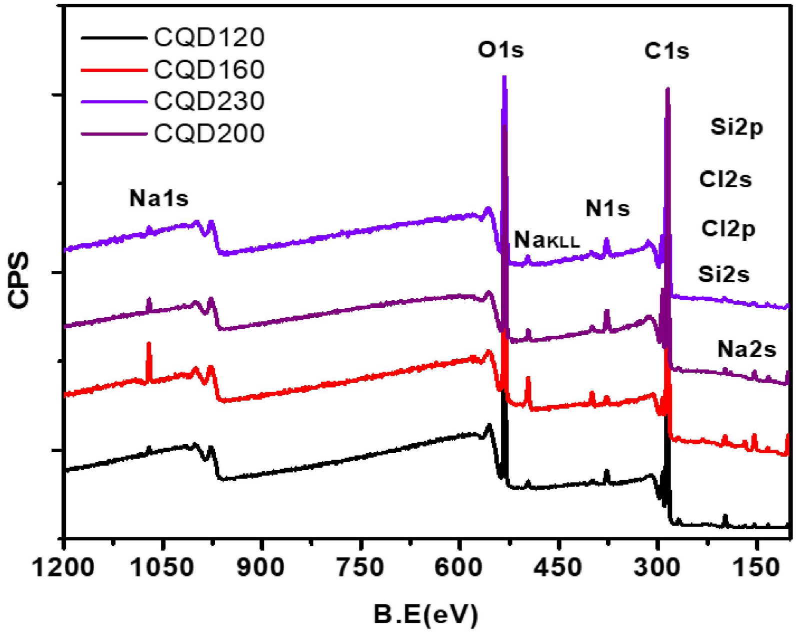

Figure 5.4 XPS survey spectrum of CQDs synthesized at different temperatures. The intense peaks in the range 150-1200 eV have been labelled in the graph, Magnesium peaks were not observed

Figure *5.3* (b), (c), and (d) show the high-resolution spectra C1s, O1s, and N1s photoelectron peaks of the CQDs as a function of synthesis temperature. We observed a drastic change in all the photoelectron peaks as the synthesis temperature is increased. Both O1s and C1s peak broadens as synthesis temperature increases indicating the presence of multiple components. All the peaks have been deconvoluted and the peak fitted components have been shown below. From Figure *5.3* (b) we observe that the C1s have multiple sharp peaks at low temperatures owing to the presence of multiple Carbon species in a different chemical environment.

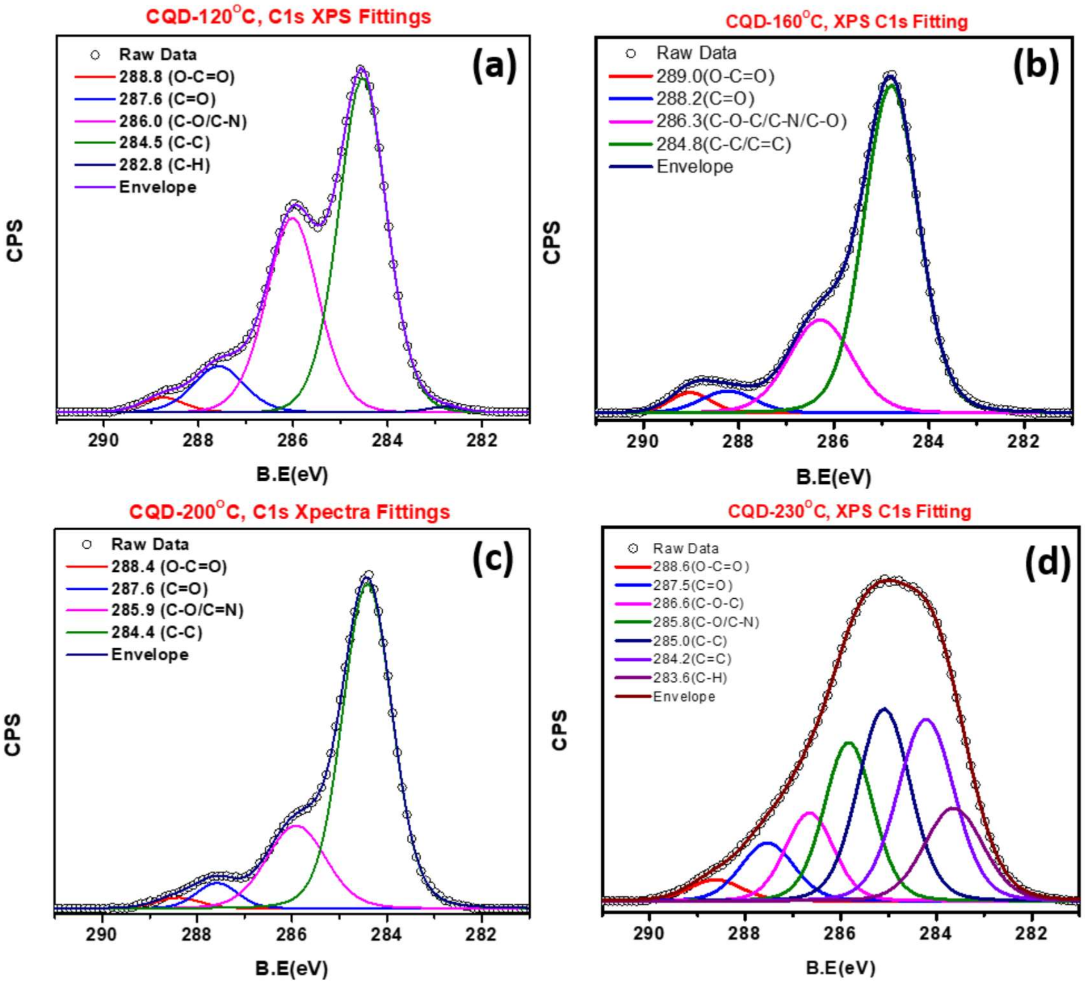

Figure 5.5 (a-d) Deconvolution of C1s photoelectron spectra CQDs synthesized at different temperatures

In Figure *5.5*, the C1s peak was deconvoluted into many species C=C, C-OH, C=O/C-N, C-O, O-C=O species. Since the peaks for C=O and C-N peaks could not be resolved we have labeled them as C=O/C-N. Figure *5.3* (c) shows the O1s spectra. At 120°C we observe a sharp O1s peak with a weak shoulder towards the lower binding energy side. As the synthesis temperatures is increased the full-width half maximum (fwhm) of the O1s peak increases and the peak shifts to lower binding energies (Figure *5.3* (c)). A broader O1s peak indicates the presence of multiple Oxygen species. From the peak fitting of O1s (Figure *5.6*) we see that O1s peak can be deconvoluted into C-OH, C=O, C-O, O-C=O, O-O species.

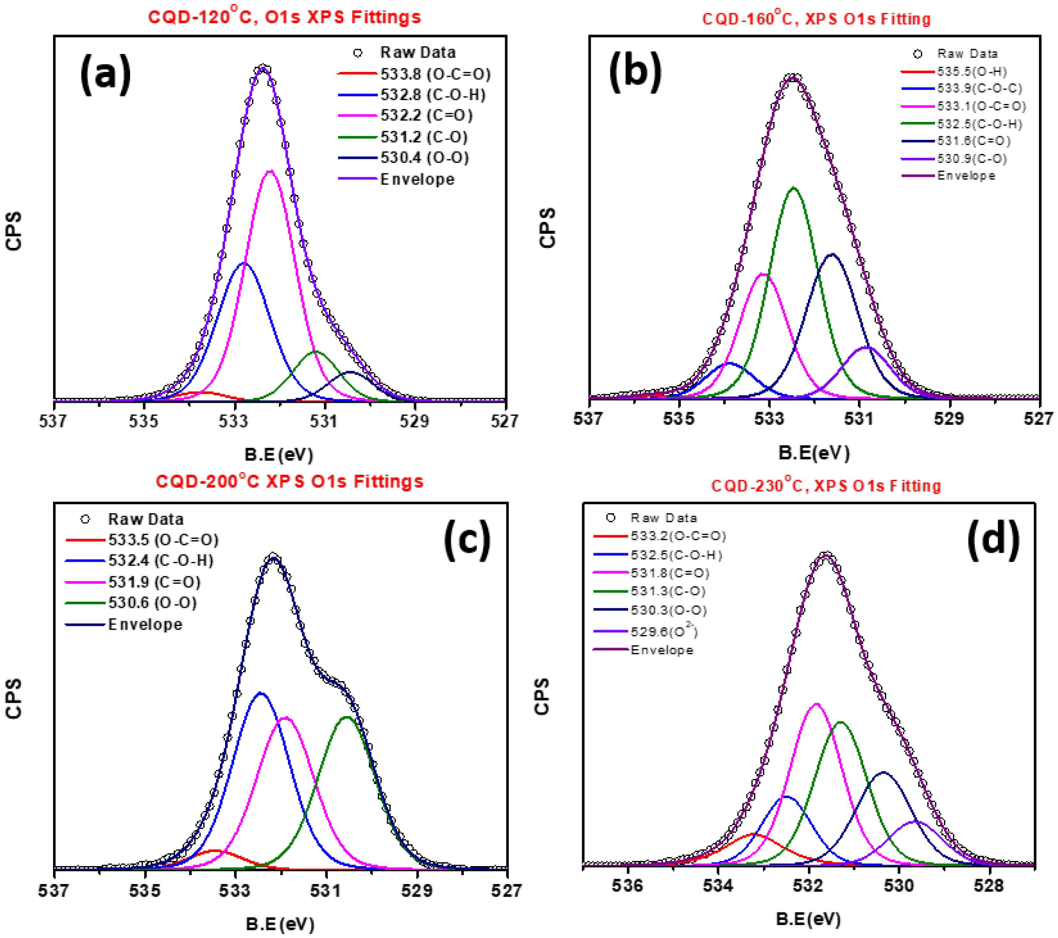

Figure 5.6 (a-d) Deconvolution of O1s photoelectron spectra CQDs synthesized at different temperatures

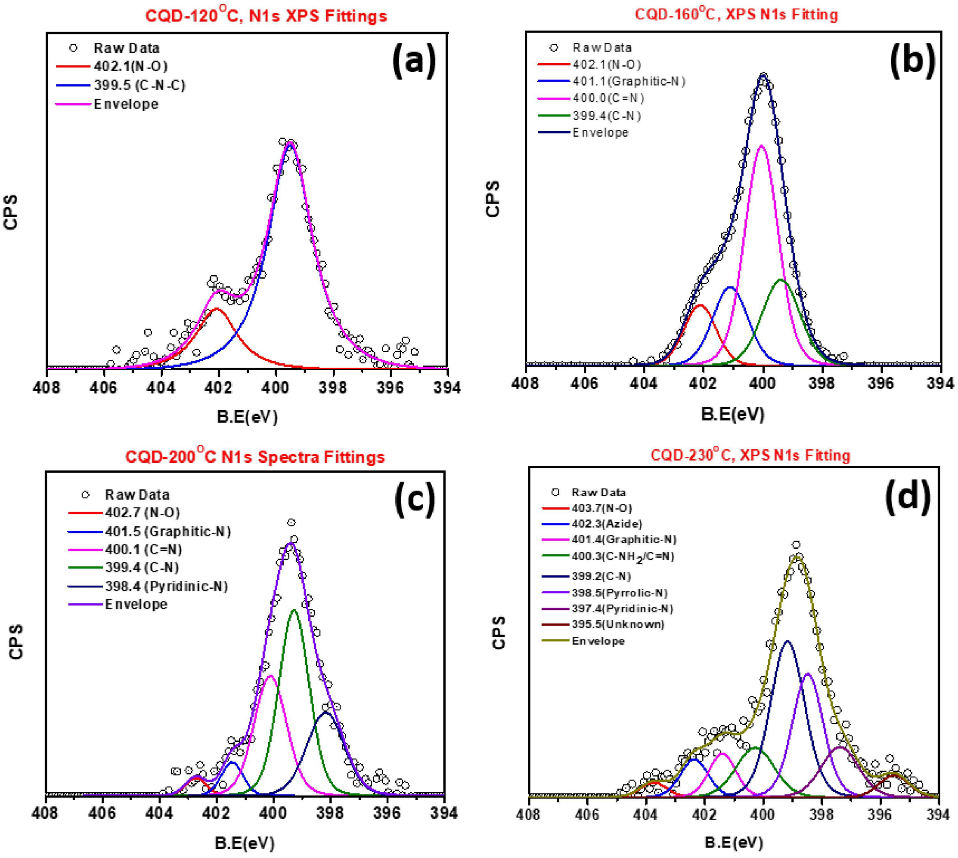

Figure 5.7 (a-d) Deconvolution of N1s photoelectron spectra CQDs synthesized at different temperatures

Figure *5.3* (d) shows the N1s spectra. For 120ºC and 160ºC the N1s peak shapes are similar and with further increase in synthesis temperatures, the N1s peaks shift to the lower binding energy. From the peak deconvolution, for the CQDs synthesized at 120°C, we observe two peaks at 399.5 eV and 402 eV for the N1s peak (Figure *5.7*). The peak at 399.5 eV can be attributed to C-N bonds. We do not observe any sign of metal (Mg^{2+}) ligated Nitrogen, which suggests that we have lost the central Mg^{2+} ion [212]. At 230°C the N1s peaks have mostly composed of graphitic, pyridinic or pyrrolic N components.

Table 5-1 summarizes all the peak positions and peak areas of C1s, O1s, and N1s. Even though there is a large number of oxygen-containing functional groups present in CQDs, the relative concentrations of different oxygen functionalities depend on the synthesis temperature. For the CQDs synthesized at 120°C the concentration of C=O groups is much larger than C-O groups, while for the CQDs synthesized at 230°C, the C-O and C=O are approximately present in the same ratio. The presence of diverse oxygen functional species on CQDs gave rise to distinct optical properties (*Table 5-1*).

Table 5-1 The C1s, O1s peak positions obtained after peak fitting. The error ± 0.2 eV for peak C1s and O1s peak

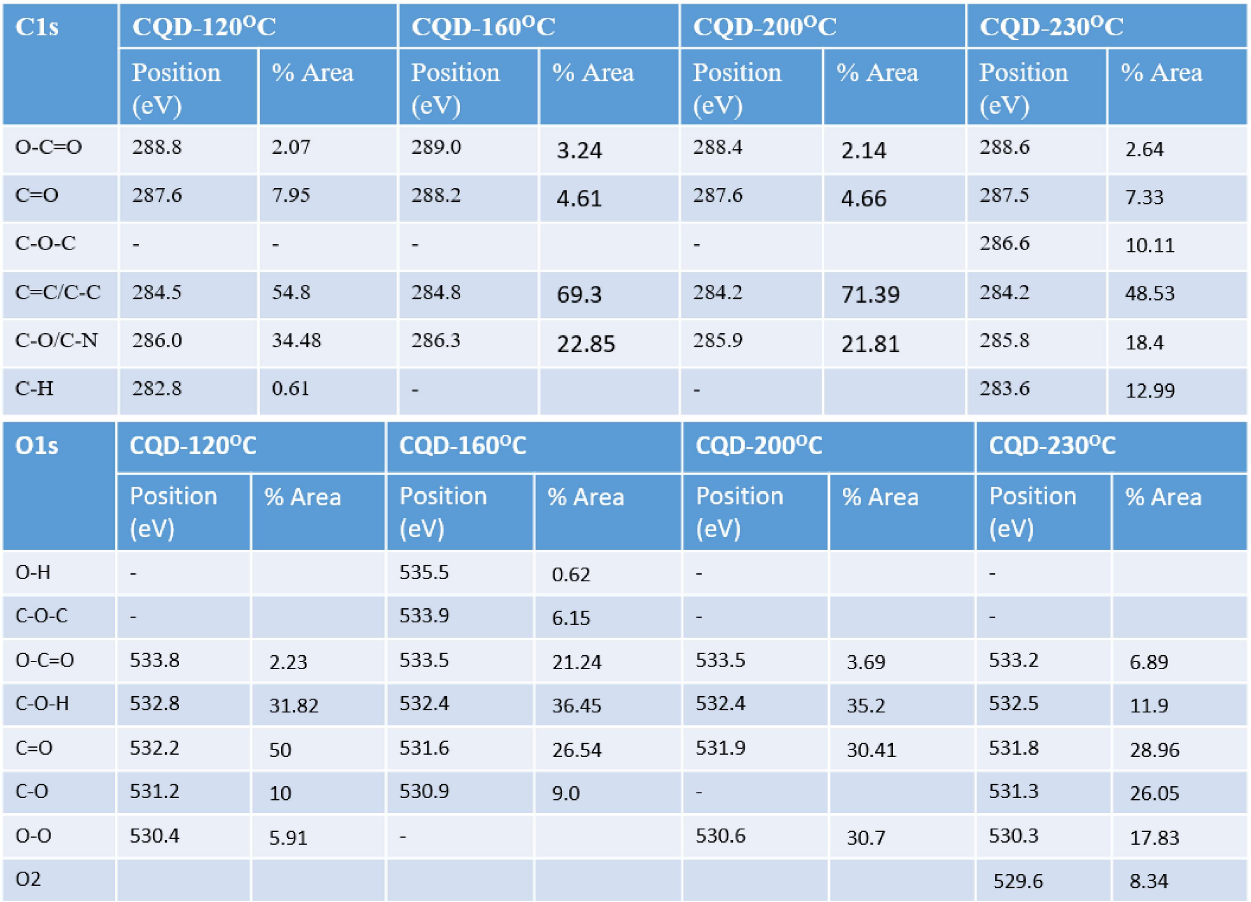

C1s	CQD-120^{o}C		CQD-160^{o}C		CQD-200^{o}C		CQD-230^{o}C	
	Position (eV)	% Area	Position (eV)	% Area	Position (eV)	% Area	Position (eV)	% Area
O-C=O	288.8	2.07	289.0	3.24	288.4	2.14	288.6	2.64
C=O	287.6	7.95	288.2	4.61	287.6	4.66	287.5	7.33
C-O-C	-	-	-		-		286.6	10.11
C=C/C-C	284.5	54.8	284.8	69.3	284.2	71.39	284.2	48.53
C-O/C-N	286.0	34.48	286.3	22.85	285.9	21.81	285.8	18.4
C-H	282.8	0.61	-		-		283.6	12.99

O1s	CQD-120^{o}C		CQD-160^{o}C		CQD-200^{o}C		CQD-230^{o}C	
	Position (eV)	% Area	Position (eV)	% Area	Position (eV)	% Area	Position (eV)	% Area
O-H	-		535.5	0.62	-		-	
C-O-C	-		533.9	6.15	-		-	
O-C=O	533.8	2.23	533.5	21.24	533.5	3.69	533.2	6.89
C-O-H	532.8	31.82	532.4	36.45	532.4	35.2	532.5	11.9
C=O	532.2	50	531.6	26.54	531.9	30.41	531.8	28.96
C-O	531.2	10	530.9	9.0	-		531.3	26.05
O-O	530.4	5.91	-		530.6	30.7	530.3	17.83
O2							529.6	8.34

5.2.3 Structural and Optical Properties of CQDs

The CQDs synthesized at 160°C were chosen as the model for further structural and optical characterization as shown in Figure *5.8*. High-resolution transmission electron microscopy (HRTEM) images show the synthesized CQDs are mostly amorphous and possess a quasi-spherical shape within the range of 2-5nm. Particles are uniformly distributed and the average size of the CQDs is 3.5nm as shown in the bar graph (Figure *5.8* (a) inset). XRD patterns of the CQDs (Figure *5.8* (b)) have a broad diffraction peak at 24° suggesting the presence of amorphous carbon dots structure while the sharp peaks observed at 28.36° and 40.62° correspond to the sp^2 hybridized graphite carbon grown along (002) and (100) crystal planes[213]. Thus at 160°C, we get a mixture of amorphous and crystalline CQDs.

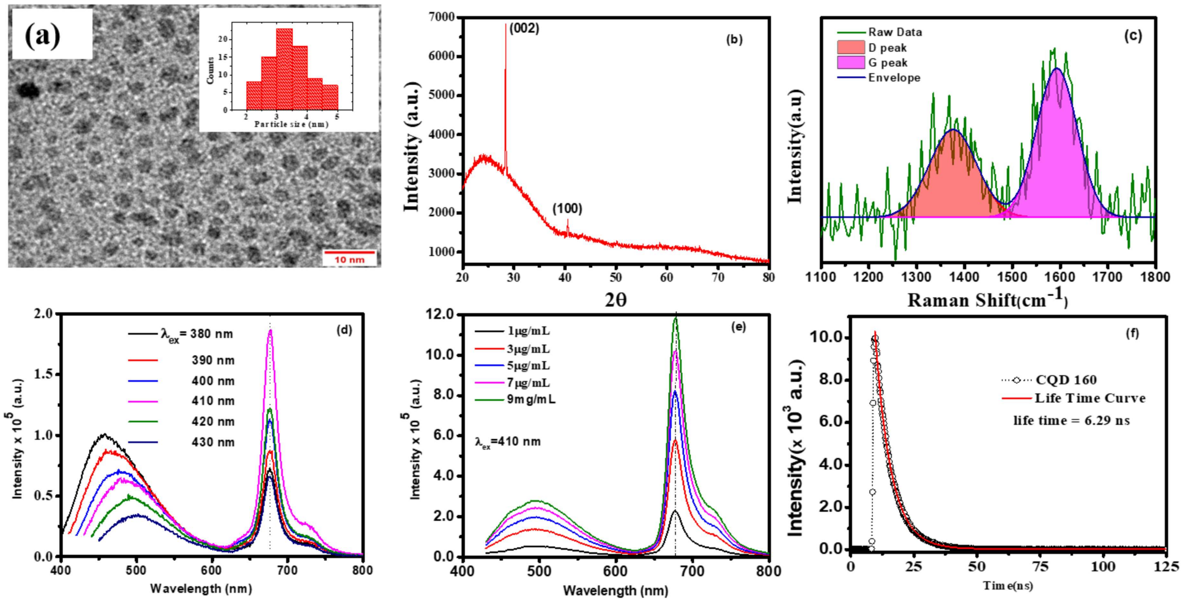

Figure 5.8 Characterization of as-synthesized CQDs (a) TEM Image of CQD Inset: Bar graph showing CQD size distribution (b) XRD pattern of CQD (c) Raman spectrum acquired with 532 nm laser excitation, (d) Excitation dependent emission spectra of 1 μg/ml CQDs in wat water (e) Concentration-dependent emission spectra of CQD at 410 nm (f) Photoluminescence lifetime measurement of CQD

Figure *5.8* (c) shows the Raman spectra of the CQDs. The Raman spectra was recorded after drop-casting the CQD solution on SiO_2/Si substrate. The spectra were deconvoluted using Lorentzian peaks. For the CQDs, we observe a peak at 1375 cm^{-1} associated with the disorder or defect-related peak (D peak) and another peak at 1593 cm^{-1} corresponds to the in-plane vibrational mode of sp^2 graphitic carbon (G peak). The D peak intensity is lower than the G peak intensity but the FWHM of the peaks is very large.These broad D and G peaks indicate the presence of a large number of defect states or surface functional groups [214]. Figure *5.8* (d) shows a detailed photoluminescence (PL) spectrum of CQDs (concentration 1μg/ml) as a function of excitation wavelengths. When the excitation wavelength is increased from 380 nm to 430 nm, the fluorescence emission peak at 495 nm gets blue-shifted with a corresponding increase in intensity. While no peak shift is observed for the emission peak at 677 nm, the intensity of this peak initially increases with an increase in excitation wavelength and then decreases, with maximum intensity at λ_{ex} = 410 nm. As mentioned earlier this peak at 677 nm corresponds to the chlorophyll moiety and has a much higher intensity than the peak at 480 nm at 410 nm excitation. Figure *5.8* (e) shows the PL spectra of the peak emission as a function of CQD concentration at 410 nm excitation. With increasing concentration of CQDs the intensity of both peaks at 480 nm and 677 nm increases. The peak at 480 nm is dispersive (shifts to a higher wavelength) while the peak at 677 nm is non-dispersive as a function of excitation wavelength. The relative quantum yield (QY) of the ChlCQD was also estimated by comparing with a standard fluorophore the Rhodamine 6G (quantum yield of Rhodamine 6G is 95%) dissolved in ethanol. QY was determined using equation (1), corresponding to an excitation wavelength of 410 nm.

$$\phi_S = \phi_R \left(\frac{I_S}{I_R}\right)\left(\frac{A_R}{A_S}\right)\left(\frac{n_S^2}{n_R^2}\right) \ldots\ldots\ldots\ldots\ldots (1)$$

where Φ, I, A, and n refer to quantum yield, integrated luminescence intensity, absorbance wavelength 410 nm, and solvent refractive index respectively. The Refractive index of water and ethanol was taken to be 1.33 and 1.36 respectively during calculation. The subscript R and S stand for reference (Rhodamine 6G) and sample (ChlCQD) respectively. The relative QY of the ChlCQDs was calculated to be ~42.2%. Figure *5.8* (f) shows the PL lifetime measurement. The photoluminescent lifetime of CQDs at room temperature was measured using 410 nm excitation. The PL decay curve was fitted using a bi-exponential function corresponding to two lifetimes $\tau_1 = 6.22\, ns$ and $\tau_2 = 18.07\, ns$ with an average lifetime of $\tau_{avg} = 6.28\, ns$ (Figure *5.8* (f)). All further sensing experiments were conducted with the CQDs synthesized at 160°C and these will be referred to as ChlCQD.

5.2.4 Sensing of Hg^+ and As^{3+} ions

The sensing property of CQDs was investigated using photoluminescence measurement. For the sensing experiment, CQDs synthesized at 160°C with a concentration of 0.02 μg mL^{-1} were used for selective detection of Hg^+ and As^{3+} metal ions. Figure *5.9* (a) shows the PL spectra of the ChlCQDs as a function of Hg^+ in the range 625 nm to 800 nm. The PL emission with the full range is shown in Figure *5.10*. Upon addition of a small amount of Hg^+ (100 pM) ions, the PL intensity at 677nm decreased a bit while the peak at 480 nm remained nearly unchanged. With further increase in the concentration of the Hg^+, the intensity at 677 nm continued to decrease until it was completely quenched beyond 20μM concentration. Figure *5.9* (c) shows the relationship between (F/F_0 -1) with Hg^+ concentration, where F_0 is the PL intensity of CQD, and F is the PL intensity of CQDs when Hg^+ ions are present at 677 nm. There is a Polynomial relationship ($R^2 = 0.98872$) between the PL intensity and Hg^+ concentration in the range of 100 pM–20 μM (Figure *5.9* (c))

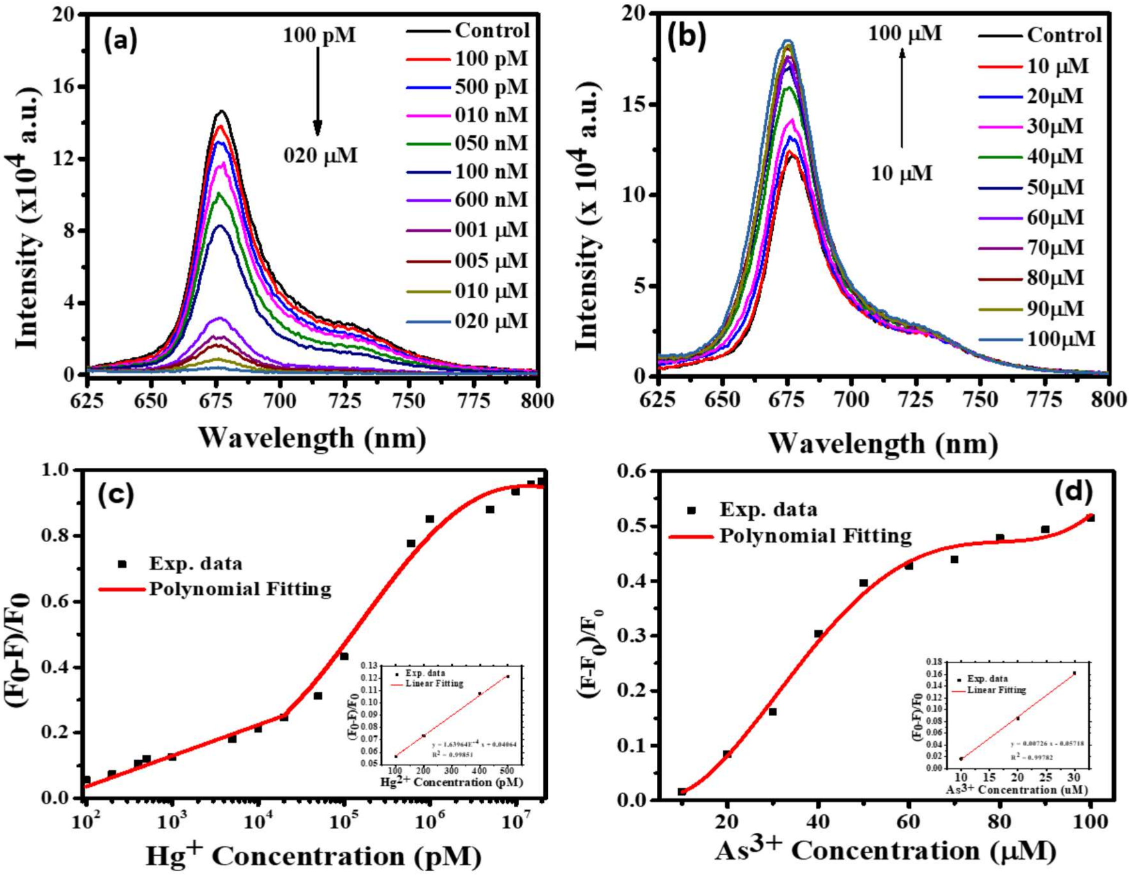

Figure 5.9 Sensing Hg^+ and As^{3+} (a) PL emission spectra of the CQD + Hg^+ system as function of [Hg^+] (b) PL emission spectra of the CQD + As^{3+} as function of [As^{3+}]. For these measurements the concentration of ChlCQDs is set at 0.02μg/ml (c)Plot of 1-(F0/F) on Hg^+ concentration within the linear range of 100 -500 pM, (d) Plot of (F_0/F)-1 versus concentration of As^{3+} and shows the linear correlation in a 10-30 μM range

For low concentration range from 100 – 500 pM, a linear relationship is observed, which was used to determine the limit of detection (LOD=3σ/m, where σ is the standard deviation of blank measurements of the composite and m represents the slope of the graph). The LOD was estimated to be 67 pM shown as shown in the inset of Figure *5.9* (c). Figure *5.9* (b) shows the PL spectra of the ChlCQDs as a function of As^{3+} concentration for 410 nm excitation. In this case, the PL intensity at 677 nm and 480 nm both gradually increased with the increase in As^{3+} concentration. The increase in the 677 nm peak is greater than the 480 nm peak. Figure *5.9* (d) shows the relationship between (F/F$_0$ -1) with As^{3+} concentration, where F$_0$ is the PL intensity of CQD, and F is the PL intensity of CQDs when As^{3+} ions are present at 677 nm. We found that polynomial relationship (R^2 = 0.98825) between the PL intensity and As^{3+} concentration in the range of 10 –100 μM (Figure *5.9* b). From the linear region between 10 – 30 μM, the LOD for As^{3+} was estimated to be 1.53 μM, shown in inset Figure *5.9* (d).

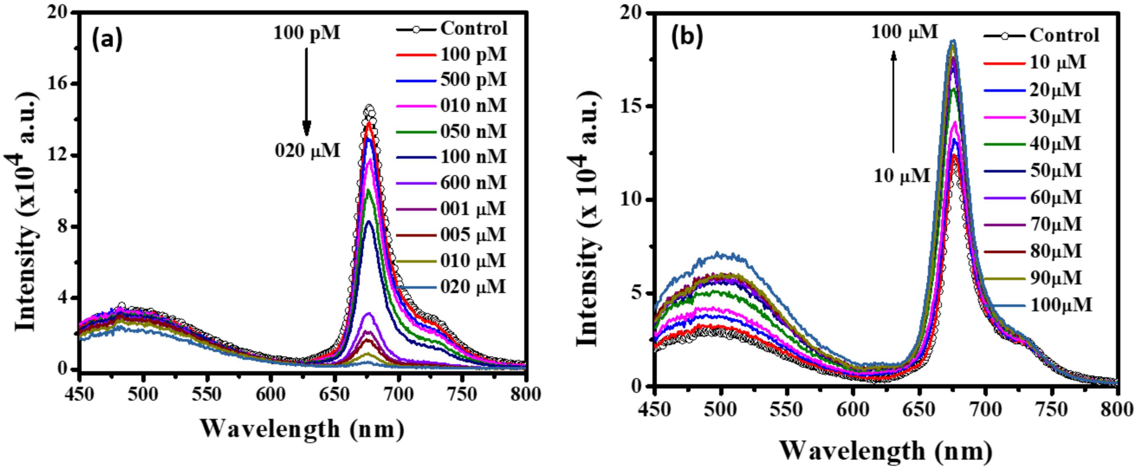

Figure 5.10 Full spectrum of CQDs sensing with Hg$^+$ and As^{3+} (a) PL emission spectra of the CQD + Hg$^+$ system as function of [Hg$^+$] (b) PL emission spectra of the CQD + As^{3+} as function of [As^{3+}]

All the above PL spectra were recorded for a ChlCQD concentration of 0.2 μg/ml. When the concentration of ChlCQDs is increased to 200 μg/ml, then fluorescence quenching by addition of 1 μM and 25 μM of Hg$^+$ and fluorescence enhancement by addition of 10 μM and 100 μM of As^{3+} can be observed directly under UV light illumination (Figure *5.11* (a), (b)). To probe the degree of selectivity, other metal ions (like Ca^{2+}, Cd^{2+}, Zn^{2+}, Ag^{+}, Pb^{2+}, Sn^{2+}, and Na^{+}) were added into the ChlCQDs solution with a final concentration of 100 μM, and then the respective PL spectra were recorded under excitation at 410 nm. From the bar graph (with the addition of metal ions Hg^{+} and As^{3+} ions) shown in Figure *5.11* (c) we observe that the PL intensity decreases remarkably with the addition of Hg^{+} ions, while the intensity increases with the addition of As^{3+} but there is no significant change for the other ions. This indicates that the ChlCQDs can act as a highly selective dual probe for Hg^{+} (OFF) and As^{3+} (ON) ions.

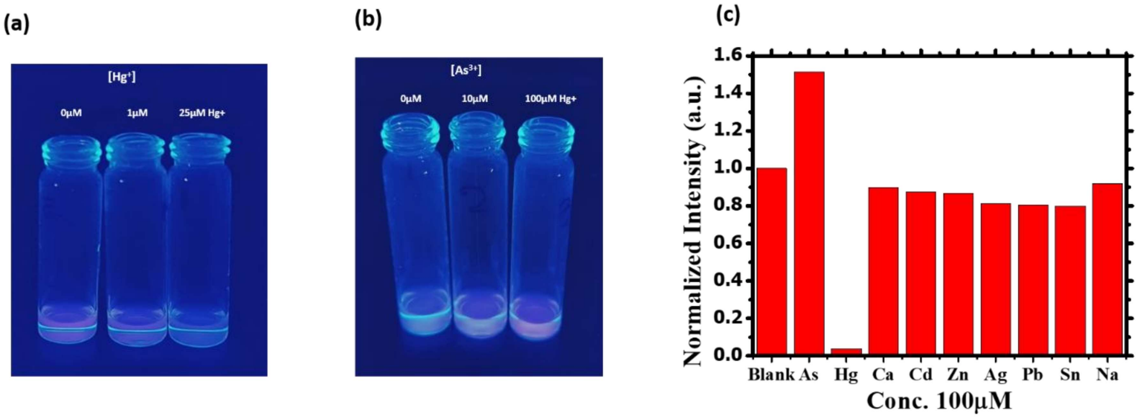

Figure 5.11 The evolution of the emission color for ChlCQDs after addition of (a) Hg^{+} and (b) As^{3+} under UV illumination (c) Histogram showing selectivity towards Hg and As ions

Our results are comparable to or better than similar sensors fabricated using CQDs from the different precursors. CQDs derived from thiol were utilized to detect As^{3+} the linear response of ions was determined over a concentration range of 5-100 ppb with a LOD value of 0.086 ppb [215]. The detection of As (III) at concentrations ranging from 1.0 to 10 nM was reported utilizing a graphene-lead oxide electrode. The detection limit for As (III) was 1.3 pM. In the presence of As^{3+} ions, this sensing system displayed efficient quenching, demonstrating the creation of metal complexes and surface contact with an oxygen functional group. The oxygen-rich GSH-CDs exhibited a higher selectivity for As^{3+} ions compared to other competing ions. The fluorescence quenching assay determined the concentration range of 2–12 nM and the detection limit to be 2.3 nM for As^{3+} [216]. Table *5-2* and Table *5-3* shows the comparison of the LOD values obtained using other sensing materials for Hg^{+} and As^{3+} detection respectively. Our results show that these ChlCQD may be useful in environmental applications for Hg^{+} and As^{3+} detection.

Table 5-2 Comparing the LOD limit of Hg^{2+} ion

Materials	**On/Off**	**Linear range**	**LOD**	**Ref.**
CQDs derived from lemmon jouce/EDTA	Turn - off	0.001–1 µM	5.3 nM	[217]
Chl-a extracted from pea leaves in ethanol	Turn - off	2.0-10 µM	1.3 µM	[218]
Spinach chl-a extracted from peanut shell	Turn - off	-	8.5 mM	[219]
CQDs derived from ginkgo leaves	Turn - off	0.5–20 µM	12.4 nM	[220]
CQDs derived from SnO2	Turn - on	0.02 - 100 µM	5 nM	[221]
CQDs derived from phosphorus, sulfur, boron, and nitrogen atom	Turn - off	0.025-1500 mM	5 µM	[222]
sulfhydryl functionalized CQDs	Turn - off	0.45 - 2.1 µM	12 nM	[223]
Our Work	Turn-off	100-500 pM	67 pM	

Table 5-3 Comparing the LOD limit of As^{3+} ion

Materials	**On/Off**	**Linear range**	**LOD**	**Ref.**
CQDs derived from thiol	Turn - off	5-100 ppb	0.086 ppb	[215]
graphene-lead oxide	Turn - off	1.0 - 10 nM	1.3 pM	[216]
oxygen-rich GSH-CDs	Turn - off	2-12 nM	2.3 nM	[216]
CQDs derived from prickly pear cactus	Turn - off	2-12 nM	2.3 nM	[216]
CQDs and guanylated Poly(methacrylamide)	Turn - off	0.01-100 nM	247 pM	[224]
MPA-capped CdTe QDs and Rhodamine 6G	Turn - on	0.02-2 µm	6 nM	[225]
CdS–MAA QDs	Turn - off	0.08-3.20 mM	0.07 mg/L	[226]
Our Work	Turn-on	10-30 µM	1.5 µM	

The CQDs synthesized at 200°C and 230°C were also tested for sensing Hg^{+} and As^{3+} ions. Figure *5.12* shows the fluorescence spectra after the addition of metal ions to CQDs synthesized at 200°C and 230°C. When As^{3+} and Hg^{+} ions are added to CQD200, both peaks at 480 nm and 677 nm get quenched, indicating that selectivity is lost. For the CQD230, the peak at 480 nm also gets quenched. Only the CQDs synthesized at 160°C is showing opposing behavior when Hg^{+} (quenching) and As^{3+} ions (enhancement) are added, which can be used to fabricate OFF and ON types of sensors to detect Hg^{+} and As^{3+}. However, the sensitivity of detection of metal ions is much higher for Hg^{+} compared to As^{3+} ions. When both Hg^{+} and As^{3+} ions are present at the same concentration, the quenching due to Hg^{+} ions should dominate. To verify this a series of control experiments was conducted where Hg^{+} ions were added to the CQD solution first and then As^{3+} ions were added. The concentration of Hg^{+} ions was kept constant at 100 nM while the concentration of As^{3+} was varied. Fluorescence spectra was recorded for mixtures of Hg^+ and As^{3+} in CQD solution with ratio of Hg^+:As^{3+} ions as 1:1,1:10,1:100, and 1:1000.

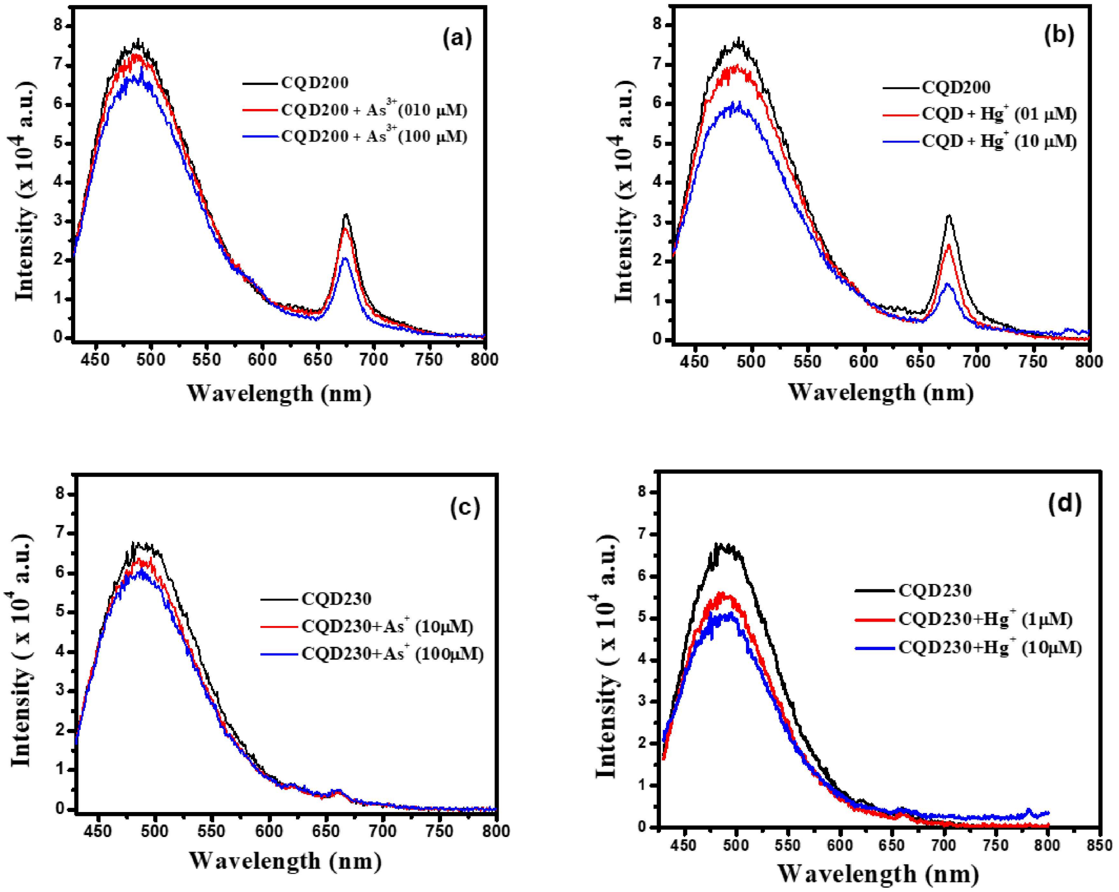

Figure 5.12 Fluorescence spectra after addition of metal ions to CQDs synthesized at 200°C and 230°C. Panel (a) and (c) is for As^{3+} while (c) and (d) is for Hg^+ ions. Excitation wavelength 410 nm

Figure *5.13* shows the emission spectra with both Hg^+ and As^{3+} ions. Only when the concentration of As^{3+} ions is 100 times or greater than Hg^+ ions, we can see an enhancement in the 677 nm peak, while for lower concentrations we observe quenching of this peak. Thus when Hg^+ and As^{3+} ions are both present in a sample, the CQDs will detect As^{3+} only when it is present at a higher concentration than Hg^+ ions.

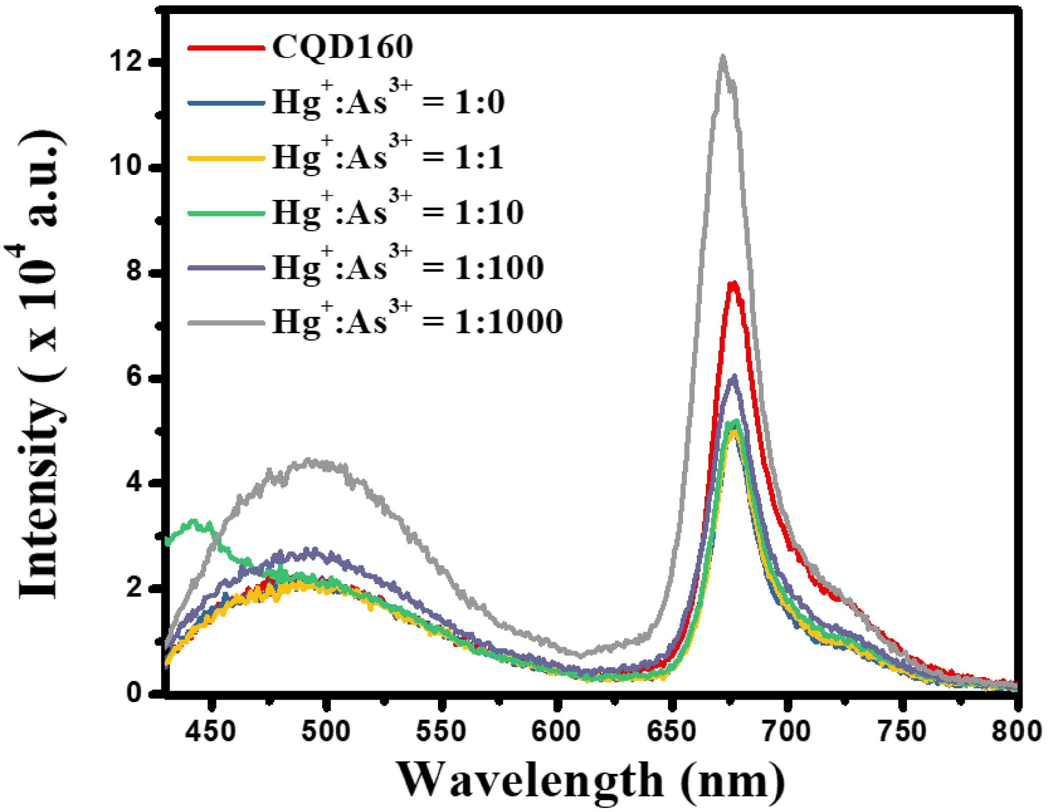

Figure 5.13 Fluorescence spectra of CQD solution with Hg^+ and As^{3+} ions

5.2.5 Test on real water sample

The sensing capability of CQDs was also tested using real water samples taken from pond water on the campus, tap water, and RO filtered water. These water samples were centrifuged and filtered to remove dissolved solid particles. They were also boiled for 2 mins to remove biological contaminants. The PL emission of different water samples with and without CQDs is shown in Figure *5.14*. The PL emission of DI water, tap water, and RO filtered water without CQDs look similar, but for the pond water sample, we observe a large peak around 480 nm (Figure *5.14* (a)).

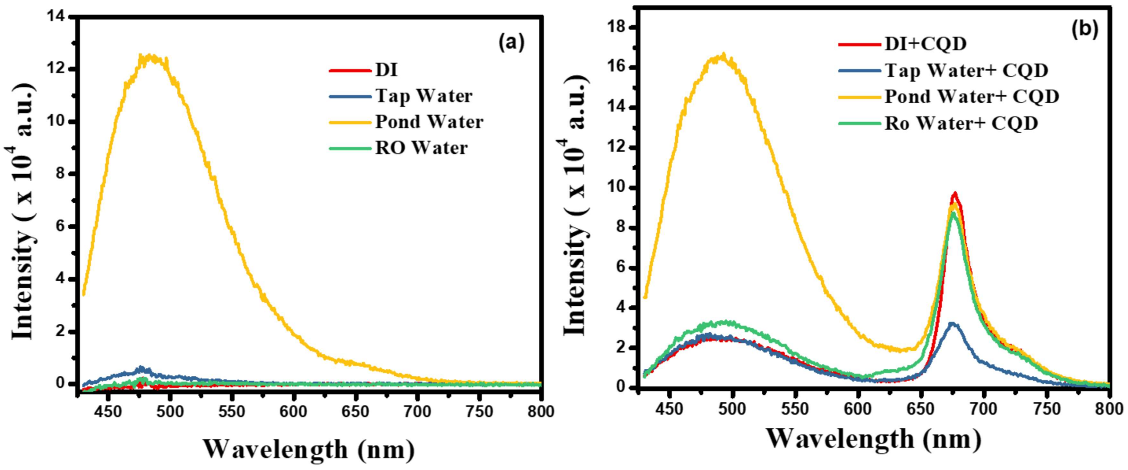

Figure 5.14 Fluorescence spectra of water samples (a) without CQDs and (b) with CQDs

The presence of a 480 nm peak indicates that CQDs may be present in the pond water or it can be due to some other fluorescent dye molecule with emission in the blue-green region [227]. When the same concentration of CQDs is added to these water samples, a new peak appears at 677 nm in addition to the 480 nm peak (Figure *5.14* (b)). Compared to DI water the intensity of the 480 nm peak for pond water is larger while the intensity of the 677 nm peak is similar. For tap water, the intensity of the 480 nm peak is comparable to that of DI water but the intensity of the 677 nm peak is decreased as compare to DI water. It indicates that Hg^+ ions are present in tap water but absent in pond water. From the calibration curve, we estimate that tap water contains about 500 nM of Hg^+ ions. For the RO filtered water, we observe that the peak at 677 nm has increased to the levels of that of the DI water, indicating that nearly all Hg^+ ions have been removed.

5.2.6 Sensing mechanism with Arsenic and mercury ions

Fluorescence enhancement or quenching has been attributed to energy transfer or an electron transfer mechanism or a combination of both [228][229]. As^{3+} and Hg^+ ions can either accept or donate electrons to the ChlCQDs to form metal complexes. It is known that divalent heavy metal ions with ionic radius in the range 75-90 pm (Hg^{2+}, Cd^{2+}, Zn^{2+}) can readily substitute Mg^{2+} in the macrocycle of chlorophyll to form heavy metal complexes [230]. However, our XPS results did not show any sign of the central Mg^{2+} ion in the ChlCQDs (Figure *5.4*) we can consider that the porphyrin macrocycle of the Chlorophyll moiety has become demetalated. Also, the As^{3+} ion having a similar size as the Mg^{+} ion, may get inserted in the cavity of the porphyrin ring and bind to the Nitrogen atoms. Due to the larger size of the Hg^{+} ion, it is unlikely to sit in the cavity of the porphyrin ring. A second possibility can be that both Hg^{+} and As^{3+} may bond with oxygen ions in the periphery of the chlorophyll molecule to give rise to peripheral complexes. A third possibility is that the metals ions bind to the oxygen and nitrogen-containing functional groups on the carbonaceous core of the ChlCQD surface. All these types of interactions would lead to metal and ChlCQD complex formation and modify the absorption spectrum. To confirm whether heavy metal ions were interacting with chlorophyll or other surface functional groups, we measured the absorbance spectra of CQDs synthesized at 160°C (ChlCQDs) and 230°C (without chlorophyll) respectively. Figure *5.15* (a) shows the UV Vis absorbance spectra of ChlCQDs synthesized at 160°C with Hg^{+} (10µM and 100 µM) and As^{3+} ion (10µM and 100 µM) respectively. When 10µM concentration of Hg^{+} and As^{3+} is added we do not observe much change from the ChlCQDs. When concentration is increased to 100 µM, for Hg^{+} ions the absorption bands from the chlorophyll moiety are nearly suppressed. In the case of 100 µM As^{3+}, we observe a new peak at 380 nm while the Q band intensity is reduced but there is no shift in the peak position. This result indicates that the As^{3+} ions are forming some kind of metal complex with ChlCQD at high concentrations. Figure *5.15* (b) shows the absorbance spectra of CQD synthesized at 230°C with Hg^{+} (10μM and 100 μM) and As^{3+} ion (10μM and 100 μM) respectively. For both Hg^{+} and As^{3+}, we observe there is not much difference in the absorbance spectra between CQD, CQD + Hg^{+}, and CQD +As^{3+} which suggests that there is no interaction between the metal ions with the carbon core or the surface functional groups of the CQDs. This shows that the As^{3+} ions are preferentially binding with the chlorophyll functional groups present in ChlCQDs while Hg^{+} has a weak interaction with the ChlCQDs.

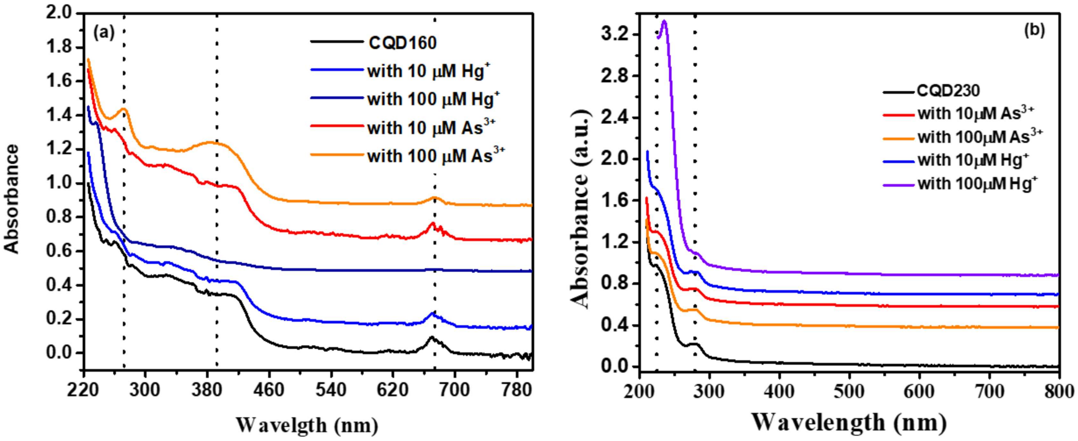

Figure 5.15 UV-Vis absorption spectra of CQDs with metal ions (a) ChlCQDs synthesized at 160°C with Hg^{+} (10,100 μM) and As^{3+} (10,100 μM) , (b) CQDs synthesized at 230°C with Hg^{+} (10,100 μM) and As^{3+} (10,100 μM)

If Chlorophyll functional groups are playing the decisive role in sensing the metal ions, then the same effect can be observed with chlorophyll molecules and there is no need for the CQDs. Gao et. al. had shown that pure chlorophyll-a pigment in ethanol (extracted from pea leaves) can be used for the detection of Hg^{2+} ions. The authors had found the linear range to be 2.0-10 μM with LOD for ions 1.3 μM. [218]. Wang et. al. had achieved trace level detection of Hg^{2+} ions with spinach extracted chlorophyll-a immobilized on peanut shell with LOD 8.5 mM [219]. However, the pure Chlorophyll-a pigment was only sensitive to Hg^{2+}ions and unresponsive to other ions. We also conducted a control experiment where the metal ions were directly added to the banana leaf extract. With the addition of metal ions (Hg^+ and As^{3+}) ions, we observed that the fluorescence intensity is getting quenched for both ions (Figure *5.16*).

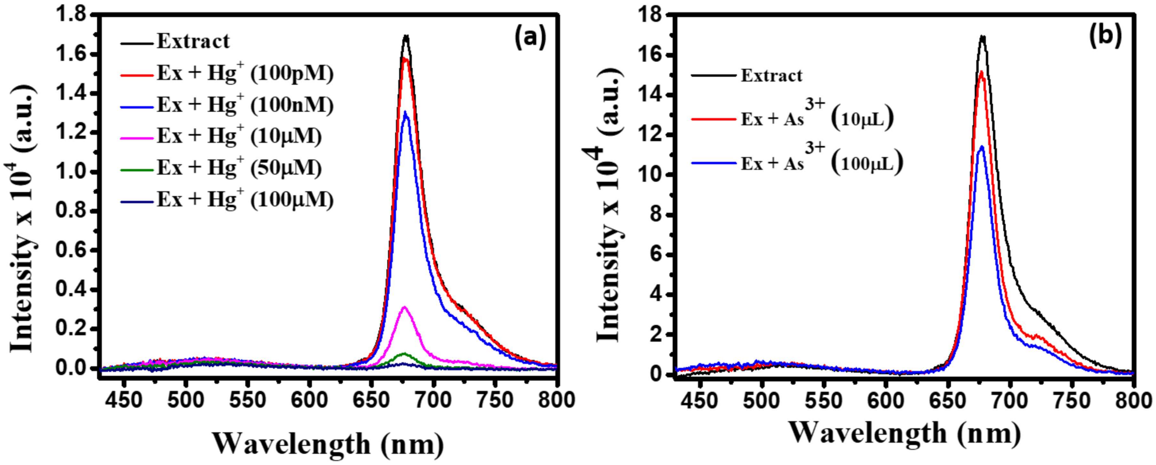

Figure 5.16 Banana Extract sensing with Hg^+ and As^{3+} (a) PL emission spectra of the Extract + Hg^+ system as function of [Hg^+] (b) PL emission spectra of the Extract + As^{3+} as function of [As^{3+}]

When the extract is used we are losing the sensitivity and specificity. The extract solution is behaving differently from the pure chlorophyll pigment, which may be due to the presence of other plant pigments in the extract solution. So the presence of CQDs help in improving the sensitivity and selectivity of detection of the metal ions. There is a synergistic effect between CQDs and chlorophyll functional group which leads to enhancement of fluorescence signal for As^{3+} ions and quenching of fluorescence for Hg^+ ions, which enables us to detect Hg^+ and As^{3+} ions. To shed more light on the chemical interaction of the metal ions with ChlCQDs, they were further characterized by XPS after the addition of As^{3+} and Hg^+ ions respectively.

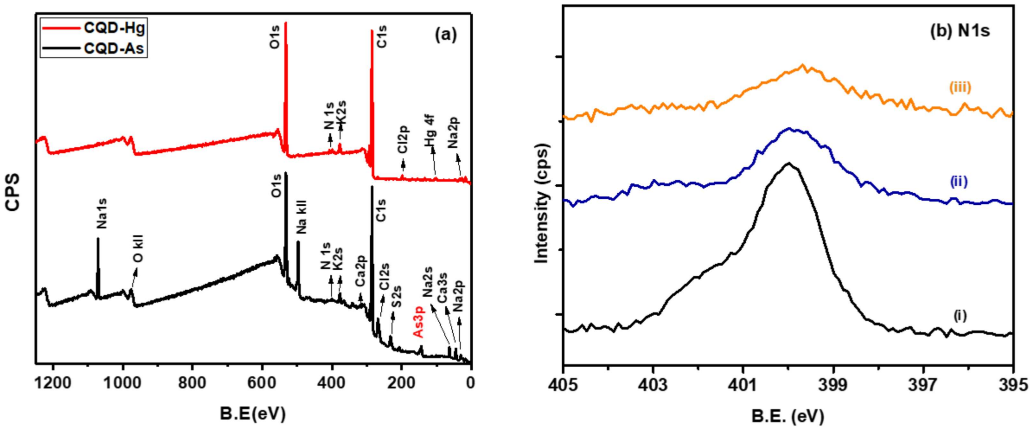

Figure 5.17 (a) XPS Survey spectrum after addition of As^{3+} and Hg^{+} (b) High resolution N1s after addition of Hg^{+} and As^{3+} ions. The spectra (i), (ii), (iii), in panels (a) and (b) correspond to ChlCQD, ChlCQD + 100 µM Hg^{+}, and ChlCQD + 100 µM As^{3+} respectively

Figure *5.17* shows the XPS survey spectra for the three cases. The XPS survey spectra of the as-synthesized of ChlCQDs show primarily C1s and O1s peaks, while for the ChlCQD + Hg^{+} and ChlCQD + As^{3+} we were able to observe small Hg and As peak. Figure *5.18* shows the high-resolution XPS spectra of C1s, O1s, Hg 4f, and As 3d peaks after the addition of Hg^{+} and As^{3+} ions. The peak shape and peak position of C1s remain nearly unchanged for both As^{3+} and Hg^{+} suggesting that there may be weak binding with carbon. In the case of As^{3+}, we observe a large change in the O1s peak shape but a small change for Hg^{+} ions, which indicates that the As^{3+} ions are binding more strongly to the oxygen-containing functional groups than Hg^{+}. The N1s peak is shown in Figure *5.17* (b).To get more information about all the different species present in O1s and C1s of the ChlCQD peak, ChlCQDs + Hg^{+} and ChlCQDs + As^{3+} fitted into multiple components. Figure *5.19* and Figure *5.20* show the deconvoluted C1s, and O1s peak after adsorption of metal ions.

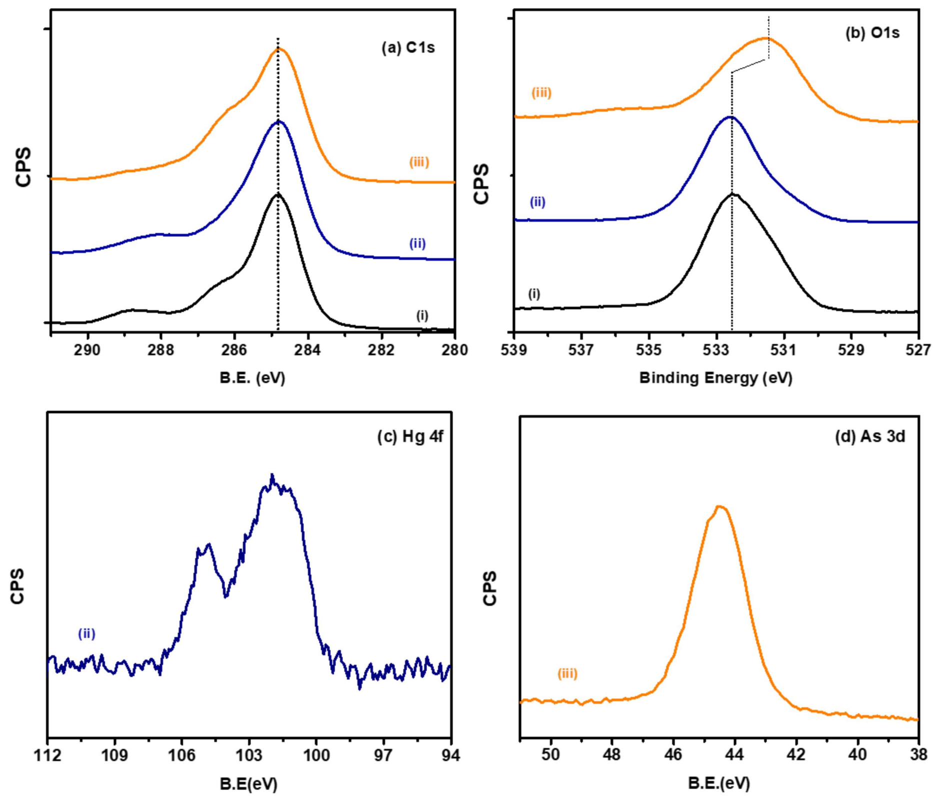

Figure 5.18 High resolution XPS spectra of ChlCQDs after addition of Hg^+ and As^{3+} ions. (a) C1s (b) O1s (c) Hg4f and (d) As3d. The spectra (i), (ii), (iii), in panels a(a) and (b) correspond to ChlCQD, ChlCQD + 100 μM Hg^+, and ChlCQD + 100 μM As^{3+} respectively

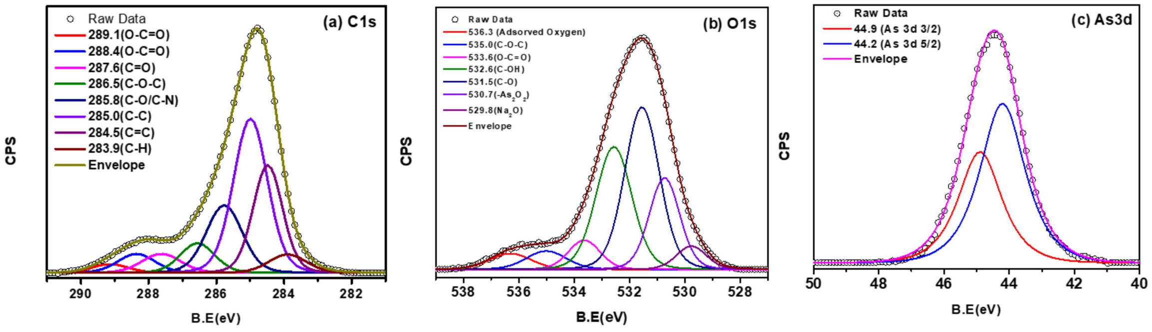

Figure 5.19 Deconvolution of (a) C1s (b) O1s and (c) As3d photoelectron peaks after addition of 100 μM As^{3+} to ChlCQDs

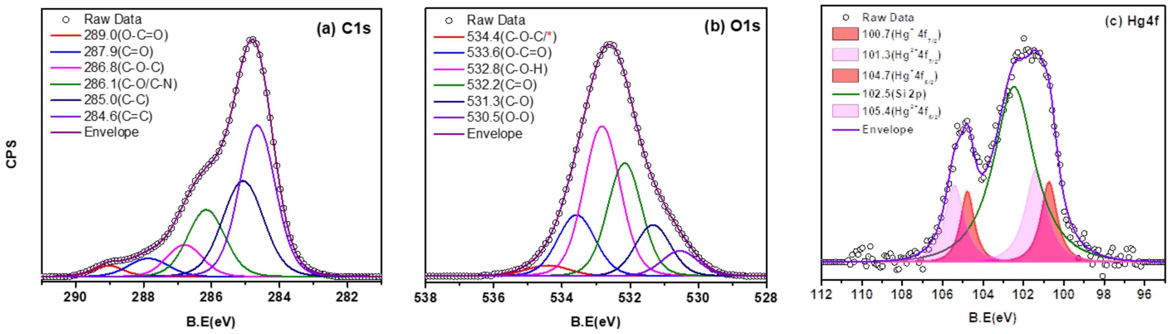

Figure 5.20 Deconvolution of (a) C1s (b) O1s and (c) Hg4f after addition of 100 µM Hg^+ ions to ChlCQDs. The Si 2p peak could not be resolved

All the different species present in C1s, and O1s along with their peak position and % area are shown in Table *5-4*. The Chlorophyll functionalized CQD (ChlCQD) synthesized at 160°C is composed of nearly 69% graphitic (sp^2) carbon but when Hg^+ and As^{3+} ions are added the sp^3 content in C1s increases. In ChlCQD, most of the oxygen functional groups is hydroxyl (C-OH), keto (C=O), and carboxyl (O-C=O) type. When As^{3+} ions are added we observe a marked decrease in the keto group and an increase in the arsenate type of species. While in the case of Hg^+ ions we do not observe too much change in the peak positions of the components in C1s and O1s peaks. When As^{3+} is added we observe new peaks corresponding to oxygen binding to arsenic at 530.7 eV.

Table 5-4 Functional groups position and area derived from XPS

Species	**Components**	**ChlCQD**		**ChlCQD + Hg^+**		**ChlCQD + As^{3+}**	
		Position	**% area**	**Position**	**% Area**	**Position**	**% Area**
C1s	O-C=O	289.0	3.24	289.0	2.5	288.4	4.93
	C=O	288.2	4.61	287.9	5.19	287.6	5.16
	C-O-C	-	-	286.8	8.09	286.5	7.14
	C-O/C-N	286.3	**22.85**	285.8	**17.73**	285.8	**16.95**
	C-C	-	-	285.0	**27.86**	285.0	**36.63**

	C=C	284.8	**69.3**	284.6	**38.63**	284.5	**22.14**
	C-H	-	-	-	-	283.9	4.84
O1s	O-H	535.5	0.62	-	-	-	-
	C-O-C	533.9	6.15	534.4	3.17	534.4	4.66
	O-C=O	533.5	**21.24**	533.6	**15.54**	**533.6**	**5.84**
	C-O-H	532.4	**36.45**	532.8	**36.76**	532.8	**27.84**
	C=O	531.6	**26.54**	532.2	**26.14**	532.2	-
	C-O	530.9	9.0	531.3	**12.18**	531.3	**35.49**
	O-O	-	-	530.5	6.21	-	-
	-As_2O_2	-	-	-	-	**530.7**	**17.61**
	Na_2O	-	-	-	-	529.8	4.40

Figure *5.18* (c) and (d) show the Hg 4f peaks and As 3d photoelectron peaks. The arsenic peak was deconvoluted into As $3d_{5/2}$ and As $3d_{3/2}$ components, at peak positions of 44.3 and 44.9 eV and with FWHM 2.2 eV respectively. The peak positions are similar to that reported for the As^{3+} oxidation state in arsenic oxides [231]. The presence of the single pair of doublets indicates that As ion is binding with mostly binding with one type of oxygenic species. Similarly, the small Hg 4f peak has been deconvoluted into a pair of doublets corresponding to Hg $4f_{7/2}$ and $4f_{5/2}$ peaks separated by 4eV. The first pair of Hg $4f_{7/2}$ and $4f_{5/2}$ peaks is at 100.7 eV and 104.7 eV respectively. The second pair of Hg $4f_{7/2}$ and $4f_{5/2}$ peaks is at 101.3 eV and 105.4 eV respectively. Guo et. al. reported that the Hg $4f_{7/2}$ peak for +1, +2 oxidation state is at 101.7 eV, 102.5 eV respectively [232]. Even though in our case the Hg $4f_{7/2}$ peaks are shifted to low binding energies we can say that Hg $4f_{7/2}$ peak at 100.7 eV corresponds to +1 while the Hg $4f_{7/2}$ peak at 101.3 corresponds to +2 oxidation state. In addition, we also observe a Si 2p peak at 102.8 eV from the underlying glass substrate. So from the UV-Vis and XPS results, we can say that the As^{3+} is binding strongly with the electron-donating carbonyl group present in the chlorophyll moiety. It gives rise to a new complex structure with the ChlCQD, which may be one of the causes behind fluorescence enhancement. As for the Hg^{+} ions, it shows a very weak type of interaction with oxygen and carbon groups and is essentially physisorbed on the ChlCQDs. Thus, the surface chlorophyll functional groups present on the CQDs improves the interaction of As^{3+} and Hg^{+} ions with ChlCQDs leading to strong enhancement or quenching of fluorescence.

5.2.7 DFT Calculations for Understanding the Interaction between the CQDs Surface and metal ions

DFT calculations were used to further understand the interaction between As^{3+} and Hg^{+} ions with the Chlorophyll functionalized CQDs synthesized at 160°C (**ChlCQD**) and CQDs synthesized at 230°C (**CQD**). The different interaction sites were chosen based on the interaction of As^{3+} and Hg^{+} with **ChlCQD** and **CQD** and are shown in Figure *5.21* (a-b). The relative interaction energies, E_{rel} were calculated as

$$E_{rel} = E_{M-Surf} - E_M - E_{Surf} \ldots\ldots\ldots\ldots\ldots.(2)$$

Where EM_{-Surf} , E_M, and E_{Surf} are the electronic energies of metal bound surface, metal, and surface respectively as shown in Eq 2. The relative interaction energies are reported in Table *5-5* for the interaction of As^{3+} and Hg^{+} with **ChlCQD** and **CQD.** The DFT calculations show that As^{3+} has six preferable interaction sites on **the ChlCQD** surface, unlike Hg^{+} and Hg^{2+} which show only one and two interaction sites respectively on **ChlCQD**. The interaction energy of As^{3+} with the center of the porphyrin cavity, Ch_C is the most favoured interaction in **ChlCQD** which suggests that As^{3+} prefers solution. With the addition of metal ions (Hg+ and As3+) ions to the porphyrin cavity even at low concentrations on low-temperature **ChlCQD** surface. The distance between As^{3+} and four nitrogens in the porphyrin cavity of chlorophyll is unequal

(1.99Å, 2.06Å, 2.16Å and 2.11Å) as shown in Figure *5.21* (a) unlike all the equidistant nitrogens at a distance of 2.05 Å from Mg^{2+} in the chlorophyll cavity (optimized structure shown in Figure *5.21* (c)).

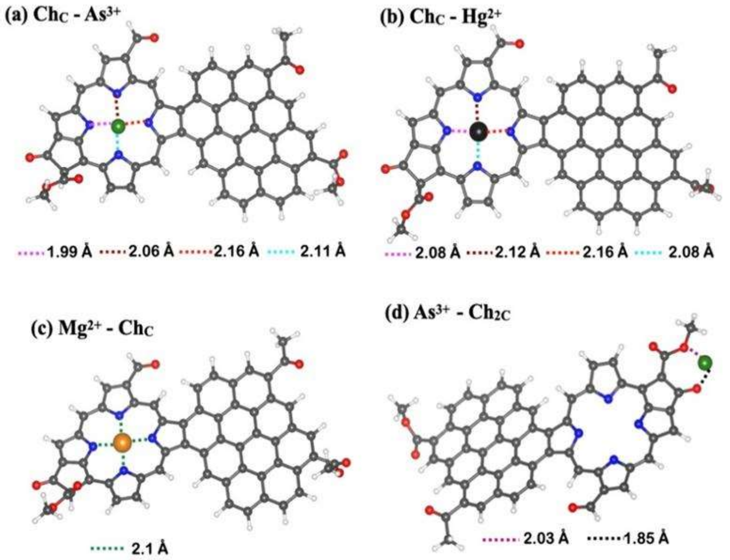

Figure 5.21 Optimized geometry of (a) As^{3+} - Ch$_C$, (b) Hg^{2+} - Ch$_C$, (c) Mg^{2+} - Ch$_C$ and (d) As^{3+} - Ch$_{2C}$ on ChlCQD; favourable N- M distances (M is metal) are shown as broken lines

Similarly, Hg^{2+} occupies the chlorophyll cavity rather than Hg^{+} and all the N-Hg^{2+} distances are unequal as reported in *Figure 5.21* (b). The asymmetrical occupancy by As^{3+} or Hg^{2+} in the cavity leads to a non-planar cavity that could lead to a less stable chlorophyll structure at high temperatures unlike the planar configuration when Mg^{2+} occupies the cavity. The experiments show no traces of Mg^{2+} in this system which suggests that Mg^{2+} is replaced by As^{3+} or Hg^{2+} in the chlorophyll cavity at low temperatures. The relative energy difference of As^{3+} with other sites is less favoured by 100 kcal/mol than As^{3+} - Ch$_C$. This suggests that other sites are the potential binding sites at higher concentrations of As^{3+}. The ester groups (Ch$_{2C}$) on chlorophyll moiety of **ChlCQD** are the second favorable sites for As^{3+} and are energetically favored by 20 kcal/mol more than the ester group on the CQD surface of ChlCQD (Ch_2). This could be due to the dichelation of As^{3+} with the oxygens of both ester and the keto groups in Ch_{2C} as shown in Figure *5.21* (d). The interaction strength of As^{3+} with CQD surface (Ch_1) and keto (Ch_3) groups on ChlCQD are similar and favorable by 17 kcal/mol then the hydroxyl group (Ch_4). This could be the reason that only the terminal hydroxyl groups on extended CQD surface bind with As^{3+} (l = 1.90 Å) unlike the hydroxyl groups that are placed in the vicinity of chlorophyll moiety where As^{3+} prefers to bind to the surface as shown in Figure *2.5* (a-b).

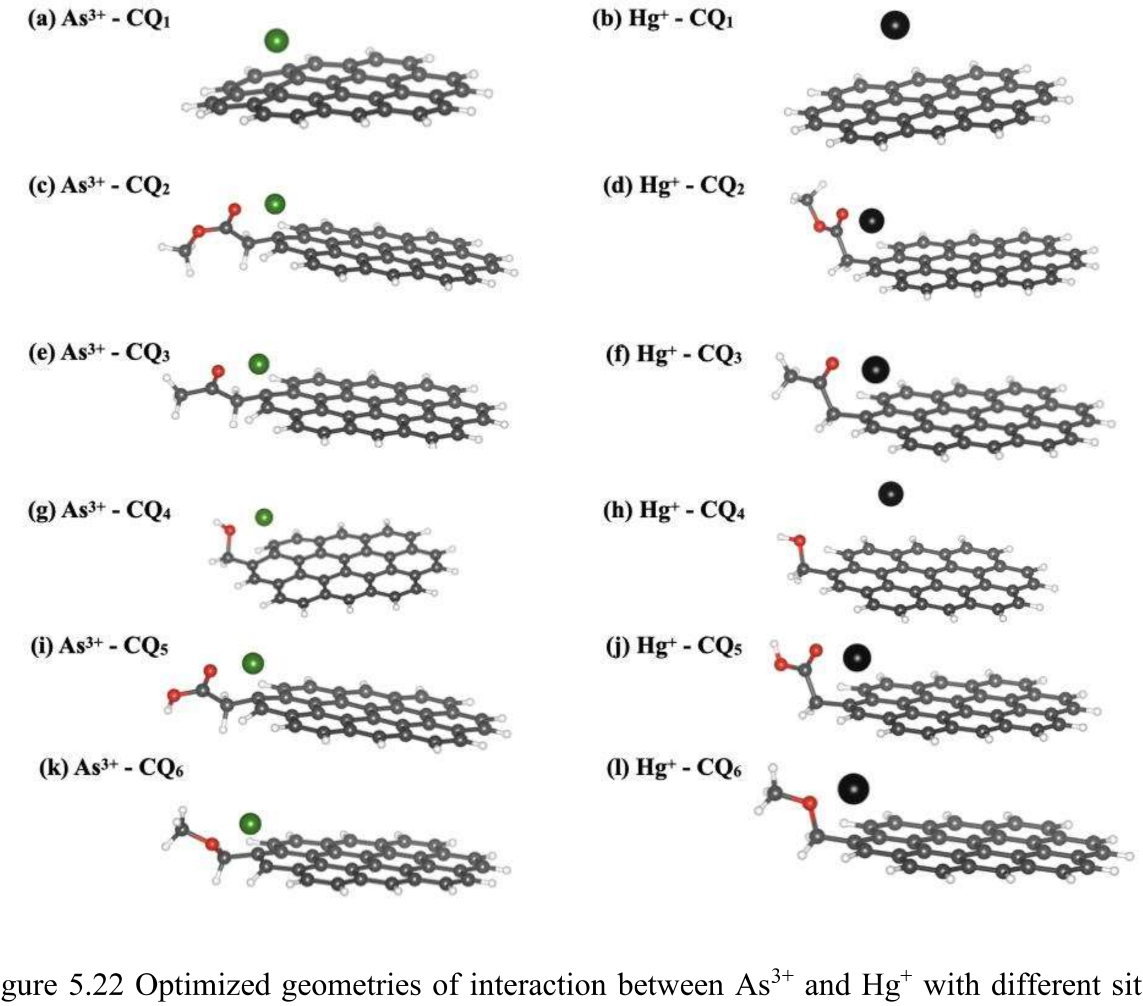

Figure 5.22 Optimized geometries of interaction between As^{3+} and Hg^{+} with different sites, CQn on CQD surface where n represents surface (n=1), ester (n=2), keto (n=3), hydroxyl (n=4), carboxylic acids (n=5) and ether (n=6) groups; centre of porphyrin ring (n=C) and ester group (n=2C) on chlorophyll moiety. The grey, white, red, green, black and blue spheres

represent C, H, O, As, Hg and N atoms. The distance between metal and site (oxygen or surface) is (a) 2.08 Å, (b) 4.03 Å, (c) 1.89 Å, (d) 2.21 Å, (e) 1.92 Å, (f) 2.21 Å, (g) 1.97 Å, (h) 5.06 Å, (i) 1.91 Å, (j) 2.24 Å, (k) 1.97 Å and (l) 2.26 Å

However, all the sites on the **CQD** model surface show interaction with both As^{3+} and Hg^{+}. The sites with oxygen-based functional groups are energetically preferred by As^{3+} than the surface of **CQD** and the sites with carbonyl functional groups are most favored in the order; ester > keto > carboxylic acid. The ether groups are favored over the hydroxyl group by As^{3+} on **the CQD** surface. However, Hg^{+} favors interaction with the hydroxyl group over the ether group. Similarly, Hg^{+} shows stronger binding with **CQD** surface than interaction with carboxylic acid and ether groups, unlike As^{3+}. The different optimized configurations of interactions between metals and **CQD** sites are reported in Figure *5.22* (a-l).

Table 5-5 Relative interaction energy of As^{3+} and Hg^{+} with different sites on ChlCQD (Chn) and (b) **CQD** (CQ$_n$) surfaces where n represents ; surface (n=1), ester (n=2), keto (n=3), hydroxyl (n=4), carboxylic acids (n=5) and ether (n=6) groups; centre of porphyrin ring (n=C) and ester group (n=2C) on chlorophyll moiety

ChlCQD **E$_{rel}$ (kcal/mol)**				**CQD** **E$_{rel}$ (kcal/mol)**		
Site	**As^{3+}**	**Hg^{+}**	**Hg^{2+}**	**Site**	**As^{3+}**	**Hg^{+}**
Ch$_1$	-718.08	-90.15	-2390.38	**CQ$_1$**	-662.77	-60.61
Ch$_C$	-875.84	-		**CQ$_2$**	-756.02	-68.57
Ch$_{2C}$	-740.98	-	-2524.4	**CQ$_3$**	-753.67	-61.09
Ch$_2$	-720.47	-		**CQ$_4$**	-715.48	-61.57
Ch$_3$	-716.85	-		**CQ$_5$**	-741.11	-59.86
Ch$_4$	-704.03	-		**CQ$_6$**	-723.25	-54.96

5.2.8 Theoretical Absorption Spectra

The theoretical absorption spectra for the interaction of metals with **ChlCQD** model surfaces is reported in Figure *5.23* (a-b). A strong absorption peak occurs due to the interaction of As^{3+} with the surface of **ChlCQD** (Ch_1) at 648 nm, unlike Hg^+ and Hg^{2+} which do not show any peak above 600nm. This is consistent with the experimentally observed diminished-absorption spectra in presence of Hg^+ as compared to As^{3+}. The electron density surfaces of HOMO → LUMO+3 transition of As^{3+} with Ch_1 in Figure *5.23* c show an effective overlap between dz^2 orbital of As^{3+} with CQD surface of **ChlCQD** and strong oscillator strength, f of 0.44 for λ = 642.7 nm. However, there is no effective overlap between Hg^+ and CQD surface in HOMO → LUMO+3 and shows negligible oscillator strength of 0.006 at 636.5 nm as reported in Figure *5.23* (d). There is a less intense peak at a larger wavelength of 429 nm (As^{3+}), 436 nm (Hg^+), 381 nm (Hg^{2+}), and 488 nm (Hg^{2+}). These peaks are consistent with high-intensity experimental peaks around 420 nm for As^{3+} and 10 mM Hg^+ on the CQD160 surface. Hg^+ and Hg^{2+} do not show any favorable interactions with oxygen-based functional groups on the **ChlCQD** surface. However, As^{3+} interacts with different functional groups and also occupies the porphyrin cavity in chlorophyll moiety and shows a broad peak at 350 nm with a shoulder at 280 nm and a low-intensity peak at 496 nm which is consistent with the weak experimental absorption peaks at 280 nm, between 500 to 600 nm and a broad experimental peak at 390 nm for 100 mM As^{3+}. The absorption spectra for the interaction of As^{3+} with ester and keto groups (Ch_{2C} and Ch_2 and Ch_3) on **ChlCQD** show a similar trend with a high-intensity peak in the range of 340 nm to 385 nm which is consistent with a broad experimental absorption peak at 390 nm due to interaction with different sites at high concentration (100 mM) of As^{3+} on CQD160. The As^{3+}- OH interactions show a peak at 410 nm and agree with a shift of the experimental peak of CQD160 from 420 nm to 410 nm. The absorption peaks for interactions of As^{3+} with **CQD** surfaces show similar absorption spectra for all the binding sites except the hydroxyl group with two peaks around 220 nm (shoulder at 252 nm) and 378 nm as shown in Figure *5.24* (a-b). A small shoulder peak at 190 nm is observed for ether (*n*=6), the carboxylic acid (*n*=5), and ester (*n*=2) sites. However, there are three absorption peaks (205, 278, and 429 nm) for As^{3+} - hydroxyl group interactions. A similar trend is observed for Hg^{+} where two peaks at 244 nm and 344 nm occur for keto, carboxylic acid, and ether functional groups and three peaks (240, 270, and 340 nm) for the hydroxyl group.

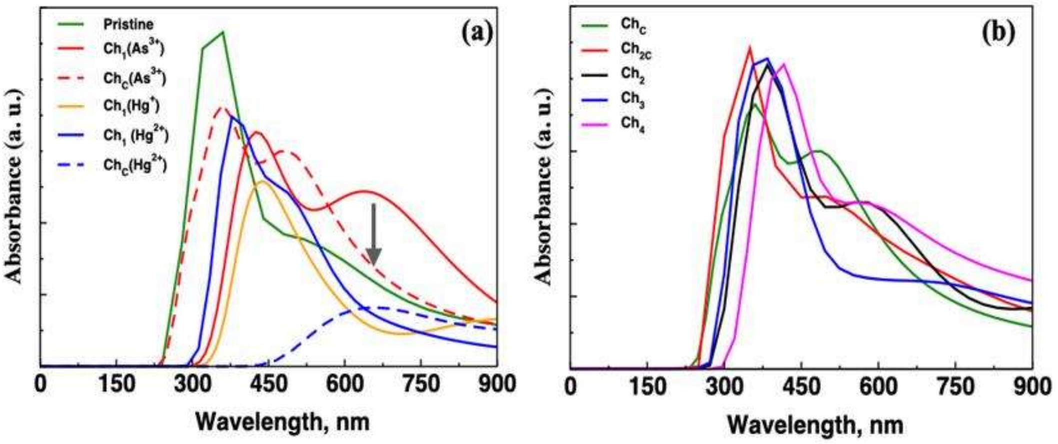

(c) As^{3+} - Ch_1 (d) Hg^{+} - Ch_1

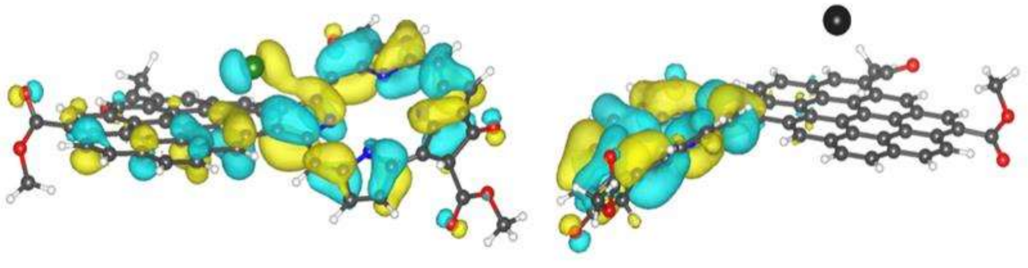

HOMO → LUMO+3 (642.7 nm, *f* = 0.44, ρ=0.02) HOMO → LUMO+3 (636.5 nm, *f* = 0.006, ρ=0.02)

Figure 5.23 Theoretical absorption spectra of (a-b) As^{3+} , Hg^{+} and Hg^{2+} on different sites (Chn) of ChlCQD; electron density surfaces for (c) HOMO → LUMO+3 of As^{3+} - Ch1 and (d)

HOMO → LUMO+3 of Hg^+ - Ch1 on ChlCQD for $\rho = 0.02$; where n represents surface (n=1)), ester (n=2), keto (n=3), hydroxyl (n=4), carboxylic acids (n=5) and ether (n=6) groups; centre of porphyrin ring (n=C) and ester group (n=2C) on chlorophyll moiety. The grey, white, red, green, black and blue spheres represent C, H, O, As, Hg and N atoms

However, there is negligible overlap between the hydroxyl group and Hg^+ as shown in Figure *5.22* (h). The intensity of peaks shows opposite trends for As^{3+} and Hg^+ where low wavelength peaks are more intense in As^{3+} and vice versa for Hg^+. On the contrary, Hg^+ shows different absorption spectra with the ester group (CQ_2) on **CQD** which is consistent with As^{3+} absorption spectra with ester groups with peaks at 194 nm, 220 nm, and 384 nm.

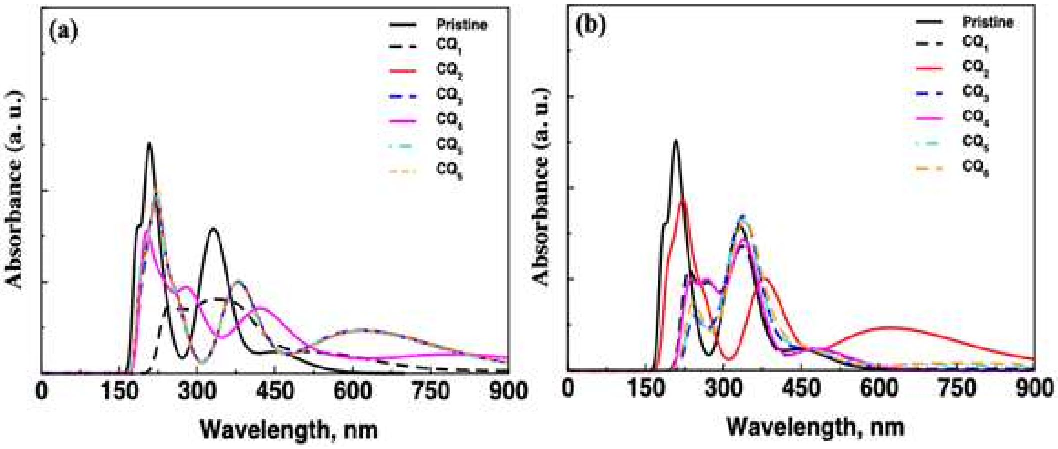

Figure 5.24 Theoretical absorption spectra of (a) As^{3+} and (b) Hg^+ on different sites, CQn of CQD surface; where n represents ; surface (n=1), ester (n=2), keto (n=3), hydroxyl (n=4), carboxylic acids (n=5) and ether (n=6) groups; centre of porphyrin ring (n=C) and ester group (n=2C) on chlorophyll moiety

5.3 Conclusion

We demonstrated the synthesis of chlorophyll functionalized CQDs using green hydrothermal synthesis. Strong temperature dependence of the carbonization and graphitization of CQDs was observed. At 160°C, chlorophyll functionalized CQDs are obtained while at 230°C, carbonization is complete so CQDs without the chlorophyll groups are obtained. These chlorophyll functionalized CQDs synthesized at 160°C were utilized to fabricate ON/OFF type of sensors for detecting As ions (+3 state) and Hg ions (in +1 / +2 states). We demonstrate that the As^{3+} binds strongly with oxygen-based functional groups on **ChlCQD** unlike mercury ions (low-temperature model structure). This interaction between As^{3+} and the surface of CQD in **ChlCQD** results in the enhancement of the fluorescence signal intensity. However, Hg^{+} and Hg^{2+} show negligible overlap with the **ChlCQD** surface which causes quenching of the fluorescence signal. Both arsenic and mercury ions show strong interaction with oxygen-based functional groups and the surface of **CQD** (high-temperature model structure) and thus, similar signal intensities for both the metal ions. Our results and analyses show that chlorophyll moiety present in CQDs synthesized at low temperatures can be used for very sensitive detection of Hg^{+} and As^{3+} ions in an aqueous medium.